



22 factors that contributed to the severe aerosol pollution event. Subsequently, with the
23 good performance of WRF-Chem model on the spatiotemporal characteristics of
24 meteorological conditions and aerosols, the trans-boundary transport flux of BC during
25 the pollution event was investigated. The results show that the vertically integrated
26 cross-Himalayan transport flux of BC decreases from west to east, with the largest
27 transport flux of $20.8 \text{ mg m}^{-2} \text{ s}^{-1}$ occurring at the deepest mountain valley in
28 southwestern TP. Results from simulations with and without aerosol-meteorology
29 feedback show that aerosols induce significant changes in meteorological conditions in
30 the southern TP and Indo-Gangetic Plain (IGP), with the atmospheric stratification
31 being more stable and the planetary boundary layer height decreasing in both regions,
32 and 10-m wind speed increasing in the southern TP but decreasing in the IGP. Changes
33 in meteorological conditions in turn lead to a decrease of surface BC concentration with
34 value up to $0.16 \text{ }\mu\text{g/m}^3$ (50%) in the southern TP and an increase of surface BC
35 concentration with value up to $2.2 \text{ }\mu\text{g/m}^3$ (75%) in the IGP. By excavating the impact
36 of aerosol-meteorology feedback on the trans-boundary transport flux of BC, it has been
37 acquired that the aerosol-meteorology feedback decreases the integrated transport flux
38 of BC from central and western Himalayas towards the TP. This study not only provides
39 crucial policy implications for mitigating glacier melt caused by aerosols over the TP,
40 but also is of great significance to the ecological environment protection for the TP.

41 **Keywords:** Tibetan Plateau; Black carbon; Transport flux; Aerosol-meteorology
42 feedback; WRF-Chem

43



44 **1 Introduction**

45 Known as “the Third Pole”, the Tibetan Plateau (TP) plays a significant role in
46 driving the climate change in the Northern Hemisphere and even the globe through
47 thermal and dynamical forcing (Lau et al., 2006;Wu et al., 2007). What’s more, with
48 the concentrated glacier and snow cover outside of the polar regions, the TP supplies a
49 substantial portion of the water demand for almost 2 billion people (Yao et al., 2022).
50 However, in recent years, numerous studies have reported that the TP experienced
51 significant and rapid climate warming during the last few decades (Kang et al.,
52 2010;You et al., 2016;You et al., 2021). As a result of this intensive warming, the
53 glaciers over the TP have undergone unprecedented widespread losses and accelerated
54 retreats (Kang et al., 2010;Yao et al., 2007). Besides high levels of greenhouse gases
55 (Duan et al., 2006), other factors like atmospheric heating and snow albedo reduction
56 due to absorbing aerosols also contribute a large portion to this climate warming and
57 glacier retreat (Xu et al., 2009;Zhang et al., 2021;Kang et al., 2019b). However, with
58 an average elevation exceeding 4 km, the TP is relatively undisturbed by human
59 activities and is one of the most pristine regions on the earth. Hence, aerosols over the
60 TP are mainly sourced from its surrounding regions (Kang et al., 2019b). Particularly,
61 with nearly half of the world’s population and heavy industry, South and East Asia
62 adjacent to the TP are the world’s hotspots for aerosol pollution (Lelieveld et al., 2016).
63 Driven by atmospheric circulation, aerosols over South and East Asia can be
64 transported to the TP, and then exert striking effect on hydrological cycle and climate
65 (Wu et al., 2008;Ramanathan et al., 2005;Liu et al., 2014). Previous studies indicated



66 that aerosols over the TP are primarily transported via the typical long-distance trans-
67 boundary transport event (Kang et al., 2019a). It is therefore paramount to excavate the
68 meteorological causes of the severe aerosol pollution event as well as the trans-
69 boundary transport flux of aerosols during the severe aerosol pollution event.

70 Black carbon (BC) exerts substantial impact on climate through several
71 mechanisms, including heating the atmosphere by absorbing shortwave and longwave
72 radiation, darkening the surface of snow and ice and accelerating the melt of cryosphere,
73 and modifying the optical and microphysical properties of clouds (Kang et al.,
74 2019b;Ramanathan and Carmichael, 2008;Flanner et al., 2007;Skiles et al., 2018).
75 Estimation from the literature shows that BC is the second most important type of
76 human forcing after carbon dioxide, with a globally climate forcing of 1.2 W m^{-2}
77 (Ramanathan and Carmichael, 2008;Chung et al., 2005). Moreover, the radiative
78 forcing of BC in snow and ice is approximately twice as high as that of carbon dioxide
79 and other types of anthropogenic forcing (Flanner et al., 2007;Qian et al., 2011;Hansen
80 and Nazarenko, 2004). Particularly, as a sensitive area to global climate change, the TP
81 has seen an increase in BC content in recent years (Xu et al., 2009). It is evident that
82 BC plays a substantial role in the climate and environmental change over the TP.
83 However, previous studies primarily focused on the origin of BC and its climatic effect
84 over the TP on annual and seasonal timescales (Yang et al., 2018;Hu et al., 2022;Rai et
85 al., 2022). With respect to the trans-boundary transport flux of BC towards the TP
86 during the severe aerosol pollution event on the synoptic scale, there is still a blank,
87 which should be studied urgently.



88 In addition, severe aerosol pollution events are usually accompanied by complex
89 aerosol-meteorology feedback. Moreover, numerous studies have revealed that the
90 aerosol-meteorology feedback has substantial effect on surface aerosol concentration
91 (Wu et al., 2019;Zhang et al., 2018;Zhao et al., 2017;Hong et al., 2020;Chen et al.,
92 2019a;Gao et al., 2015a). For instance, some studies analyzed the aerosol-meteorology
93 feedback and its effect on surface PM_{2.5} concentration during heavy aerosol pollution
94 events in winter in northern China, and found that positive aerosol-meteorology
95 feedback can increase the surface PM_{2.5} concentration (Li et al., 2020;Qiu et al.,
96 2017;Wu et al., 2019). Nonetheless, some other studies suggested that the aerosol-
97 meteorology feedback can reduce the surface PM_{2.5} concentration in Beijing (Gao et al.,
98 2015a;Zheng et al., 2015). Based on the in-situ observational data, Zhong et al., (2018)
99 analyzed the aerosol-meteorology feedback during several air pollution events in
100 Beijing and indicated that 70% of the increase in surface PM_{2.5} concentration in the
101 cumulative outbreak stage of haze could be attributed to the aerosol-meteorology
102 feedback. The above mentioned studies are mainly focused on the economically
103 developed central and eastern China; however, the TP, which has a very high altitude
104 and complex topography along with tough environment and scarce in-situ observational
105 data, systematic and comprehensive studies on aerosol-meteorology feedback and its
106 effect on surface BC concentration are still lacking, which need urgent investigation.
107 Furthermore, what effect the aerosol-meteorology feedback having on the trans-
108 boundary transport flux of BC also remains unclear, which is also worthy in-depth study.
109 Therefore, in this study, we attempt to investigate the meteorological causes, the trans-



110 boundary transport flux of BC, and the aerosol-meteorology feedback as well as its
111 effect on the trans-boundary transport flux of BC during one severe aerosol pollution
112 event by using observational and reanalysis dataset, and numerical simulation with the
113 advanced regional climate-chemistry model, the Weather Research and Forecasting
114 with Chemistry (WRF-Chem). This study not only provides crucial policy implications
115 for mitigating glacier melt caused by aerosols over the TP, but also is of great
116 significance to the ecological environment protection for the TP. This paper is
117 organized as follows. Section 2 introduces data used in this study, the definition of
118 aerosol pollution event, WRF-Chem model, and experimental details. Section 3
119 investigates the meteorological causes, the trans-boundary transport flux of BC, and the
120 aerosol-meteorology feedback as well as its effect on transport flux of BC during the
121 severe aerosol pollution event. Section 4 presents the main conclusions.

122 **2. Data, Definition of aerosol pollution event, and WRF-Chem** 123 **model and**

124 *2.1 Data*

125 *2.1.1 ERA-Interim*

126 To explore the meteorological causes of the severe aerosol pollution event, the
127 geopotential height, air temperature (T), and wind fields at 500 hPa with a horizontal
128 resolution of $0.05^{\circ} \times 0.05^{\circ}$ during the period from April 20 to May 10, 2016 are from the
129 European Center for Medium-Range Weather Forecasts interim reanalysis (ERA-
130 Interim). To evaluate the model performance on meteorology, 2-m air temperature (T2),



131 2-m dew point temperature, 10-m wind speed (U10), and wind fields at 500 hPa with a
132 horizontal resolution of $0.05^{\circ} \times 0.05^{\circ}$ are also obtained from ERA-Interim. It should be
133 noted that 2-m relative humidity (RH2) used to validate model performance is
134 calculated by 2-m dew point temperature and T2.

135 *2.1.2 AERONET*

136 The identification of aerosol pollution events on the TP is based on quality-assured
137 data from the Aerosol Robotic Network (AERONET), which was established by the
138 U.S. National Aeronautics and Space Administration (NASA) (Holben et al., 1998) and
139 is used to retrieve aerosol properties via sun photometers (Dubovik and King, 2000).
140 AERONET data, including instantaneous data and daily average by calculating the
141 diurnal average of the instantaneous values (Holben et al., 1998), are available at three
142 levels: level 1.0 (unscreened), level 1.5 (cloud-screened), and level 2.0 (cloud-screened
143 and quality assured data) (Smirnov et al., 2009). In this paper, the aerosol optical depth
144 (AOD) and fine-mode AOD at a standard wavelength of 500 nm used to define the
145 aerosol pollution event are based on the Spectral Deconvolution Algorithm (SDA)
146 version 3, level 2.0 (O'Neill et al., 2003; O'Neill et al., 2008). In addition, this kind of
147 AOD data was also used to verify the model performance on the temporal variation of
148 AOD at different sites over the study area.

149 *2.1.3 MODIS*

150 The Moderate Resolution Imaging Spectroradiometer (MODIS) instrument
151 aboard the Terra and Aqua satellites are designed with 36 spectral bands ranging from



152 0.4 to 15 μm and a high spatial resolution for retrieving reliable and extensive
153 information about solar radiation, atmosphere, ocean, cryosphere, and land. The
154 enhanced Deep Blue aerosol retrieval algorithm has substantially improved the
155 collection 6 aerosol product over the entire land region, especially in deserts and urban
156 regions (Hsu et al., 2013). Herein, to verify the model performance on the spatial
157 distribution of AOD, the AODs based on the Deep Blue algorithm at 550 nm with a
158 horizontal resolution of $1^\circ \times 1^\circ$ and a daily temporal resolution from MODIS/Aqua
159 Level-3 collection 6 products during the period from April 20 to May 10, 2016 are used.
160 It should be noted that MODIS onboard the Aqua satellite passes over the equator at
161 13:30 local time.

162 *2.1.4 MERRA-2*

163 The second Modern-Era Retrospective analysis for Research and Applications
164 (MERRA-2), which is introduced to replace the original MERRA reanalysis because of
165 the advances in the Goddard Earth Observing System Model, Version 5 (GEOS-5) data
166 assimilation system, is a NASA atmospheric reanalysis, beginning in 1980 (Gelaro et
167 al., 2017). MERRA-2 is the first long-term global reanalysis to assimilate space-based
168 observations of aerosols, including assimilation of AOD retrieved from the Advanced
169 Very High Resolution Radiometer instrument over the oceans (Heidinger et al., 2014),
170 the MODIS (Levy et al., 2010), non-bias-corrected AOD retrieved from the Multiangle
171 Imaging SpectroRadiometer (Kahn et al., 2005) over bright surfaces, and ground-based
172 AERONET observations (Holben et al., 1998). This dataset includes all the processes



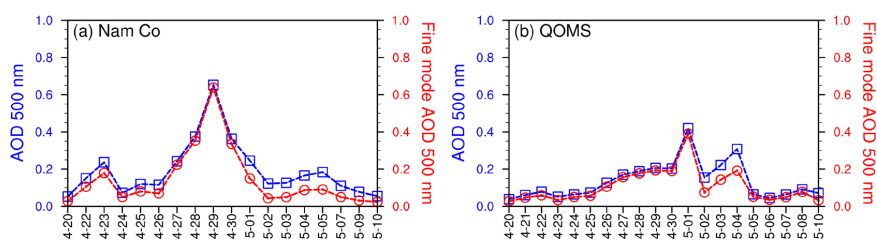
173 of aerosol transport, deposition, microphysics, and radiative forcing and has
174 considerable skill in showing numerous observable aerosol properties (Gelaro et al.,
175 2017;Randles et al., 2017), including dust, sulfate, organic carbon, BC, and sea salt
176 aerosols (Chin et al., 2002;Colarco et al., 2010). As the first long-term aerosol
177 reanalysis dataset, MERRA-2 has been adequately evaluated in previous studies
178 (Buchard et al., 2017;Che et al., 2019;Sun et al., 2019). In this paper, the hourly surface
179 BC concentration (kg/m^3), which has a spatial resolution of longitude-by-latitude grid
180 of approximately $0.625^\circ \times 0.5^\circ$, is used to validate the model performance on BC.

181 *2.2 Definition of aerosol pollution event*

182 The two main reference sites used in this study are Nam Co Monitoring and
183 Research Station for Multisphere Interactions (Nam Co), situated in inland TP
184 (30.77°N , 90.96°E , 4730 m a.s.l.), and Qomolangma Station for Atmospheric and
185 Environmental Observation and Research (QOMS, 28.36°N , 86.95°E , 4276 m a.s.l.),
186 located on the northern slope of Mt. Everest in the central Himalayas. The Nam Co and
187 QOMS stations joined the AERONET network in 2006 and 2009, respectively, and are
188 continuously functioning up to date. Both stations are background stations with less
189 human activities and can be regarded as a representative site for the inland of TP and
190 the southern TP, respectively (Pokharel et al., 2019). Figure S1 in the supporting
191 information (SI) shows daily mean of AOD at a standard wavelength of 500 nm lying
192 above the 95th percentile at Nam Co and QOMS stations since 2006 and 2009,
193 respectively. As can be seen, the observed most severe aerosol pollution event ever
194 recorded in the remote TP occurred during the period from April 27 to May 4, 2016,



195 persisting at least eight days simultaneously at Nam Co and QOMS sites. Figure 1
196 presents the temporal variation in daily mean AOD and fine-mode AOD at 500 nm for
197 both stations during the period from April 20 to May 10, 2016. Notably, the changes in
198 daily mean AOD and fine-mode AOD are synchronized and the value of daily mean
199 fine-mode AOD is very close to that of daily mean AOD, indicating that the fine
200 particulate matter dominated this severe aerosol pollution event. Meanwhile, it is also
201 acquired from Figure 1 that the most polluted period during this pollution event is from
202 April 27 to May 4. Specifically, at Nam Co station, the observed highest daily mean
203 AOD and fine-mode AOD with values of 0.65 and 0.64 appeared on April 29, 2016,
204 while at QOMS station, the measured highest daily mean AOD and fine-mode AOD
205 with values of 0.42 and 0.39 occurred on May 1, 2016. According to the previous study,
206 the baseline values of AOD at Nam Co and QOMS are 0.029 and 0.027, respectively
207 (Pokharel et al., 2019). Thus, the observed highest AOD at Nam Co and QOMS stations
208 during this severe aerosol pollution event is at least one order of magnitude than that of
209 baseline.



210
211 Figure 1 Time series of daily mean AOD (blue) and fine-mode AOD (red) at 500 nm at
212 Nam Co (a) and QOMS (b) stations during the period from April 20 to May 10, 2016.

213



214 *2.3 WRF-Chem Model Configuration, Experimental Design and Emissions*

215 The WRF-Chem model is a fully coupled regional dynamical/chemical transport
216 model that considers gas-phase chemistry, photolysis, and aerosol mechanism (Grell et
217 al., 2005). The model can simulate the emission, transport, mixing, chemical reactions,
218 and deposition of trace gases and aerosol simultaneously with the meteorological fields.
219 It has been successfully applied in air pollution studies over the TP and adjacent regions
220 (Yang et al., 2018; Chen et al., 2018; Hu et al., 2022). The version used in this study is
221 based on v3.9.1. As shown in Figure 2, the simulation domain is centered at 31°N,
222 87.5 °E, covering the whole TP and its surroundings. The model simulations are
223 conducted at a 15-km horizontal resolution using a Lambert conformal mapping with
224 259 (west-east) × 179 (north-south) grid cells. There are 30 vertical sigma levels for all
225 grids, extending from the surface to 50 hPa. The key physical parameterization options
226 used in this study include the Noah land surface model (Ek et al., 2003; Chen et al.,
227 2010) and the Monin-Obukhov scheme for the surface layer physical processes
228 (Srivastava and Sharan, 2017), the double-moment Morrison microphysical
229 parameterization (Morrison et al., 2009) with the Grell-Freitas (GF) cumulus scheme
230 (Grell and Freitas, 2014), the Mellor-Yamada-Janjic (MYJ) planetary boundary layer
231 scheme with local vertical mixing (Janjić, 1994), and the Rapid Radiative Transfer
232 Model for General circulation models (RRTMG) coupled with the aerosol radiative
233 effect for both longwave and shortwave radiation (Iacono et al., 2008). In respect to the
234 chemical parameterization options, the Carbon-Bond Mechanism version Z (CBMZ)
235 gas-phase chemistry mechanism (Zaveri and Peters, 1999) combined with the Model



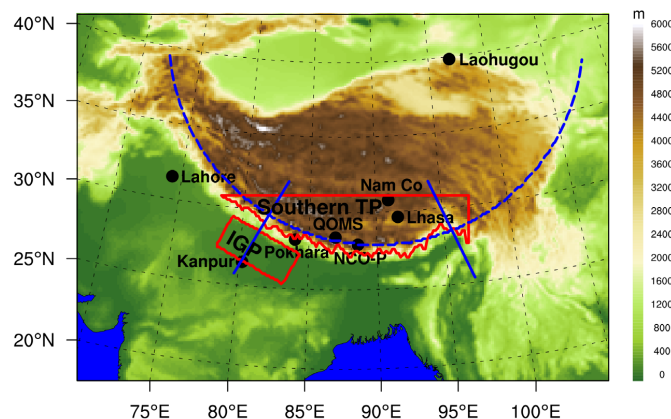
236 for Simulating Aerosol Interactions and Chemistry (MOSAIC) aerosol module (Zaveri
237 et al., 2008) was chosen for aerosol simulation. The MOSAIC aerosol scheme uses an
238 approach of segmentation to represent aerosol size distribution with four or eight
239 discrete size bins (Fast et al., 2006). In this paper, the aerosol size is divided into four
240 bins. Aerosol species simulated by MOSAIC scheme include sulfate, methanesulfonate,
241 nitrate, chloride, carbonate, ammonium, sodium, calcium, BC, primary organic mass,
242 liquid water, and other inorganic mass.

243 The initial and boundary conditions for meteorological fields are obtained from
244 the National Centers for Environmental Prediction (NCEP) Final Analysis (FNL) data
245 with a $1^\circ \times 1^\circ$ spatial resolution and a 6-h temporal resolution
246 (<https://rda.ucar.edu/datasets/ds083.2/>). Anthropogenic emissions, such as CO, VOCs,
247 NO_x, NH₃, BC, OC, SO₂, PM_{2.5}, and PM₁₀, are taken from the Emission Database for
248 Global Atmospheric Research (EDGAR)-Hemispheric Transport Air Pollution version
249 2 (HTAPv2) emission inventory (https://edgar.jrc.ec.europa.eu/dataset_htap_v2) for the
250 year 2010. Detailed information on the HTAP inventory can be found in Janssens-
251 Maenhout et al. (2015). The biogenic emissions are based on the Model of Emissions
252 of Gases and Aerosols from Nature (MEGAN) (Guenther et al., 2006; Guenther et al.,
253 2012), and the biomass burning emissions were calculated with the high resolution fire
254 emissions based on the Fire INventory from NCAR (FINN) (Wiedinmyer et al., 2011).
255 In addition, the mozbc utility and the Community Atmosphere Model with
256 Chemistry (CAM-chem) (Buchholz et al., 2019) dataset are used to create improved
257 chemical initial and boundary conditions. The simulation is conducted from April 10,



258 2016 to May 10, 2016, and the first ten days is used for model spin-up. The results from
259 April 20, 2016 to May 10, 2016 are used for the analysis.

260 A total of two experiments are designed in this study, one is a control experiment
261 (CONT) and the other is a sensitive experiment (SEN). In the CONT, the simulation is
262 conducted using WRF-Chem model with aerosol-meteorology feedback turned on. The
263 SEN is exactly the same as CONT except that the feedback between aerosol and
264 meteorology is turned off. The difference between CONT and SEN is considered as
265 effect induced by aerosol-meteorology feedback.



266
267 Figure 2 WRF-Chem model domain and terrain (shading; m). Black solid dots indicate
268 stations used to verify model performance on meteorological conditions and aerosols.
269 The solid red lines and its inner area denote the southern TP and Indo-Gangetic Plain.
270 The blue dashed line and two solid lines represent the cross sections for analysis in the
271 following.

272



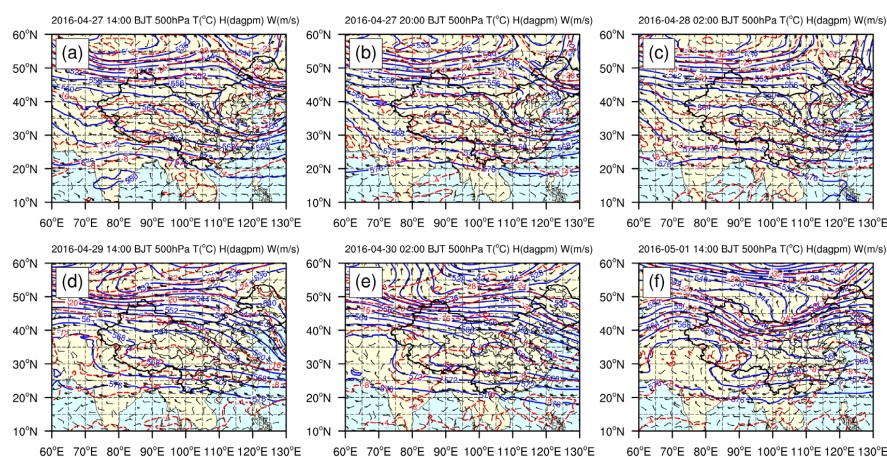
273 **3 Results and discussion**

274 *3.1 Meteorological causes of the severe aerosol pollution event*

275 Excessive emissions and adverse meteorological conditions are the two most
276 important factors influencing air quality (Zhang et al., 2019; Wang et al., 2019; Chen et
277 al., 2019b; Liu et al., 2017). The TP, which has a small population density and a low
278 degree of industrialization, is one of the most pristine regions on the earth. Moreover,
279 as mentioned above, AOD at background stations of Nam Co and QOMS with less
280 human activity is significantly higher than that of baseline from April 27 to May 4,
281 2016, with the highest value at least one order of magnitude than that of baseline.
282 Therefore, it can be inferred that aerosols over the TP during this severe aerosol
283 pollution event are mainly sourced from adjacent regions by long-range transport,
284 which is consistent with the results reported in a previous study (Kang et al., 2019b).
285 In fact, atmospheric circulation, as the main driving force of atmospheric aerosols, plays
286 a substantial role in the long-range transport of aerosols. Therefore, with little change
287 in emission source, analyzing the meteorological conditions during the severe pollution
288 event is very crucial. Figure 3 shows weather maps at 500 hPa based on ERA-Interim
289 reanalysis dataset. It is found that, during 08:00–14:00 Beijing Time (hereafter BJT) on
290 April 27, straight westerly airflow prevailed at 500 hPa over the TP (Figure 3a), which
291 transported aerosols from northwestern South Asia to the TP. Subsequently, wind field
292 shear occurred over the plateau at 20:00 on April 27 (Figure 3b), and plateau vortex
293 generated at 02:00 on April 28 (Figure 3c), which is conducive to the accumulation of
294 aerosols in the inland of the plateau. From 08:00 on April 28 to 08:00 on April 29, the



295 plateau vortex stabilized over the TP, and the aerosol concentrations at Nam Co station
296 continued increasing (figure not shown). At 14:00 on April 29, the plateau vortex
297 disappeared (Figure 3d) and the aerosol concentrations peaked at Nam Co station.
298 Meanwhile, a high-pressure system was located to the west side of the plateau
299 accompanied by a trough in the foreside (Figure 3d). Thus, southwesterly airflow in
300 front of the trough transported aerosols from northern South Asia to the southern TP
301 (Figure 3e). As a result, the aerosol concentrations at QOMS station increased and
302 peaked on May 1. At 14:00 on May 1, the high-pressure system moved eastward from
303 the west side to the inland of the TP and northerly winds ahead this high-pressure
304 system prevailed over the TP (Figure 3f), which wafted aerosols away from the TP and
305 aerosol concentrations at QOMS station began to decrease.



306

307 Figure 3 Weather maps at 500 hPa over the study area during the severe aerosol
308 pollution event based on ERA-Interim. The blue lines are isopleths of geopotential
309 height (unit: dagpm), the red lines are isotherms (unit: °C), and wind speed (unit: m/s)
310 and direction were denoted by wind barb.



311

312 *3.2 Evaluating model performance on meteorology and chemistry*

313 *3.2.1 Validation of model performance on meteorology*

314 Validating model performance on meteorology is critical for assuring accuracy in
315 simulating aerosol concentrations. This is because meteorological conditions are
316 closely associated with aerosol growth, transport, and deposition. Herein, to validate
317 the model performance on meteorological conditions, the temporal variation in the
318 simulated and reanalyzed T2, RH2, and U10 at Nam Co, QOMS, Kanpur, and Lahore
319 stations are shown in Figure S2 in the SI. The model reasonably represents the correct
320 temporal trend of T2 at four stations although underestimations are detected at Nam Co
321 and QOMS stations. The variation trend of RH2 from simulation is in high consistent
322 with that from reanalysis at Kanpur and Lahore stations. However, at Nam Co and
323 QOMS stations, a relatively larger discrepancy is observed between simulation and
324 reanalysis, which might be related to the high altitude and complex topography there.
325 For U10, the simulated trend on average coincides with the observed trend at Nam Co,
326 Kanpur, and Lahore stations. The corresponding statistics, including sample size (N),
327 observed mean, simulated mean, mean bias (MB), normalized mean bias (NMB), root
328 mean square error (RMSE), and correlation coefficient (R) between observation and
329 simulation at different stations are shown in Table S1 in the SI. The calculations
330 indicate that T2 is well simulated with MB of -4.25 , -3.62 , 0.03 , and 0.07 , and R of
331 0.69 , 0.87 , 0.94 , and 0.96 at Nam Co, QOMS, Kanpur, and Lahore, respectively. RH2
332 and U10 are less well simulated, especially at Nam Co and QOMS stations, where the



333 altitude is very high and the terrain is fairly complex. To be exact, RH2 with MB of
334 29.68 and -25.82 and R of 0.51 and 0.52 are obtained at Nam Co and QOMS,
335 respectively. And U10 with MB of 0.91 and 5.66 and R of 0.30 and 0.55 are detected
336 at two stations accordingly. However, at Kanpur and Lahore stations, RH2 and U10
337 from reanalysis and simulation are in high consistence, with MBs of -12.56 and 0.85,
338 -13.00 and 0.96, Rs of 0.80 and 0.45, 0.78 and 0.22, respectively. As a whole, U10 is
339 on the average overestimated, and has a greater range of about 3.43–8.56 m/s compared
340 to reanalyzed values with a range of about 2.47–3.39. Hence, the simulations are bias
341 at least in part since the model grid represents a regional average at $15 \times 15 \text{ km}^2$ in a
342 domain of great topographic complexity, and the values derived from reanalysis
343 represent a regional average of a relatively higher resolution. In addition, the accuracy
344 of the gridded observational data of ERA-interim is correlated with the restriction of
345 the observations assimilated into the reanalysis and with the different assimilation
346 methods (Chung et al., 2013). Overall, we conclude that the WRF-Chem model exhibits
347 acceptable performance in simulating temporal variations in meteorological elements.

348 The spatial distributions of T2, RH2, and wind field at 500 hPa from simulation
349 and reanalysis over the domain are presented in Figure S3 in the SI. Spatially, both
350 simulation and reanalysis show similar spatial patterns for each of the above mentioned
351 meteorological field. Exactly, surface air temperature with high values mainly appears
352 over regions surrounding the TP, especially obvious over South Asia where surface air
353 temperature exceeds $30 \text{ }^\circ\text{C}$. Previous studies indicated that surface air temperature over
354 the Indian subcontinent is the highest during the pre-monsoon season because the



355 Himalayas block the frigid katabatic winds flowing down from Central Asia during this
356 period (Ji et al., 2011). In contrast, surface air temperature with low values mainly
357 occurs over the TP. Different from T2, RH2 with high values primarily appears over
358 the TP, the Bay of Bengal, and central and eastern China but with low values in the rest
359 area of the domain. Particularly, RH2 in the southeastern TP is apparently higher than
360 that of the inland TP, because the southeastern TP is proximity to the moisture sourced
361 from the Bay of Bengal. Moreover, the reason why the spatial distribution of T2 is
362 antiphase with that of RH2 is that the decrease in T2 can lead to a decrease in the
363 saturation pressure of water vapor and an increase in RH2 at the surface (Gao et al.,
364 2015b). In respect to 500 hPa wind field, both simulation and observation show that the
365 westerly winds prevail over the entire region. Due to the high topography of the TP,
366 such westerly winds are divided into two branches at appropriately 75 °E. One branch
367 flow eastward, and the other branch is forced up by the high plateau and subsequently
368 shifts to northwesterly wind. Therefore, the WRF-Chem model also effectively
369 simulates the spatial distributions of T2, RH2, and 500 hPa wind field. Overall, this
370 simulation configuration captures the meteorological fields well, which is critical to
371 assure simulation accuracy of air pollutant concentrations.

372 *3.2.2 Validation of model performance on AOD and BC*

373 To validate the model performance on simulating spatiotemporal variations in
374 aerosols, AOD data from AERONET are compared to those from simulation firstly.
375 Figure S4 shows the temporal variations in simulated and observed daily mean AOD at
376 Nam Co, QOMS, and Pokhara stations for the period from April 20 to May 10, 2016.



377 As a whole, the WRF-Chem model reasonably reproduces the temporal variations in
378 AOD at each of the above stations, with relatively larger bias at Nam Co and Pokhara
379 stations and minor bias at QOMS station. The specific statistics for N, observed mean,
380 simulated mean, MB, NMB, RMSE, and R between observed and simulated AOD at
381 different stations are shown in Table S2 in the SI. The results indicate that MB with
382 values of -0.13 , -0.01 , and -0.57 , R with values of 0.58 , 0.42 , and 0.56 are obtained at
383 Nam Co, QOMS, and Pokhara, respectively. Moreover, the AOD from observation is
384 significantly correlated with that from simulation at Nam Co and Pokhara stations, with
385 correlation coefficient passing the 95% confidence level. In addition, we note that the
386 AOD from simulation is on the average lower than that from observation, which may
387 be due to the assumed spherical aerosol particles in the model simulation. Actually the
388 optical properties of particles are more sensitive to non-spherical morphology than
389 primary spherical structure (China et al., 2015; He et al., 2015). On the whole, the model
390 effectively reproduces the observed temporal variation in AOD.

391 Spatially, AOD from both simulation and observation shows distinct spatial
392 distribution characteristics (Figure S5). The simulated and observed high AOD values
393 appear over northern South Asia, the Bay of Bengal, Southeast Asia, and the Sichuan
394 Basin, but low AOD values occur over the TP. This is because South Asia, Southeast
395 Asia, and Sichuan Basin are heavily industrialized and densely populated regions
396 compared to the TP (Bran and Srivastava, 2017). In the Taklimakan Desert, AOD
397 monitored by satellite is much higher than that obtained from simulation, which might
398 be likely due to the uncertainty of the emission inventory. The comparison between



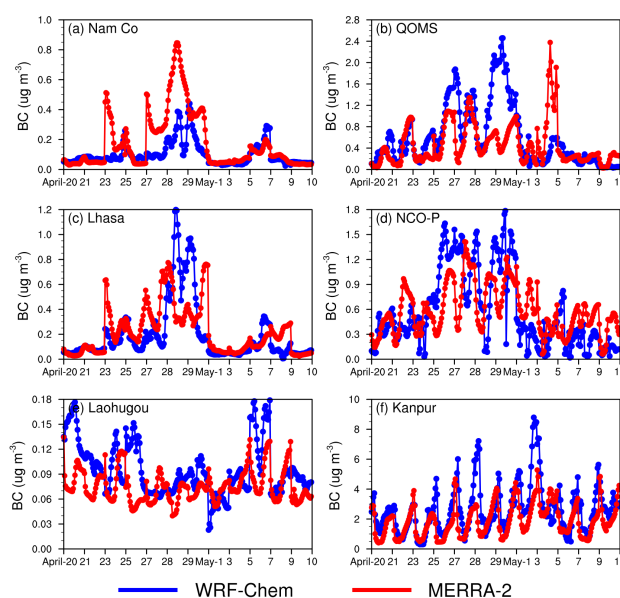
399 simulation from WRF-Chem and observation from MODIS and AERONET shows that
400 the WRF-Chem model captures the overall spatio-temporal characteristics of AOD over
401 the domain.

402 To verify the capability of this framework of WRF-Chem on simulating BC
403 concentration, we present the temporal variation in simulated and reanalyzed hourly
404 BC concentration at Nam Co, QOMS, Lhasa, NCO-P, Laohugou, and Kanpur stations
405 during the period from April 20 to May 10, as shown in Figure 4. It is found that the
406 WRF-Chem model overall reproduces the temporal variation in reanalyzed BC
407 concentrations at different stations. The specific statistics for N, observed mean,
408 simulated mean, MB, NMB, RMSE, and R between reanalyzed and simulated BC
409 concentrations at different stations are shown in Table S2 in the SI. As can be seen, MB
410 with values of -0.07 , 0.14 , -0.02 , -0.02 , 0.02 , and 0.72 , and R with values of 0.67 ,
411 0.43 , 0.47 , 0.50 , 0.25 , and 0.64 are obtained at Nam Co, QOMS, Lhasa, NCO-P,
412 Laohugou, and Kanpur, respectively. The BC concentrations from simulation are
413 strongly correlated with those from reanalysis at each of the stations, with correlation
414 coefficient exceeding the 99% confidence level. Hence, the WRF-Chem model exhibits
415 a better performance in simulating BC concentrations.

416 Figure S6 presents the spatial distributions of simulated and reanalyzed BC
417 concentrations over the domain. It can be found that BC concentrations from both
418 simulation and reanalysis display distinct spatial variability, with low concentrations
419 over the TP and high concentrations over north of South Asia, Southeast Asia, and
420 Sichuan Basin. As one of the most pristine regions on the earth, the TP has a small



421 population density and a low degree of industrialization. Nonetheless, regions like north
422 of South Asia, Southeast Asia, and Sichuan Basin with low elevation surrounding the
423 TP have dense population and developed industrialization (Li et al., 2016a; Qin and Xie,
424 2012; Li et al., 2016b), emitting large amounts of BC into the atmosphere. Therefore,
425 the WRF-Chem model can capture the main temporal and spatial features of BC
426 concentrations over the TP and adjacent regions.



427

428 Figure 4 Temporal variations in simulated and reanalyzed hourly BC concentrations at
429 Nam Co (a), QOMS (b), Lhasa (c), NCO-P (d), Laohugou (e), and Kanpur (f) stations
430 for the period from April 20 to May 10, 2016.

431

432 3.3 Trans-boundary transport flux of BC

433 The foregoing analysis has validated the model framework used in this study and
434 the results are basically satisfactory. BC, as the major component of light absorbing



435 particles, exerts a significant impact on climatic and cryospheric changes over the TP
436 due to its strong light absorption and important effect on snow and ice albedo (Kang et
437 al., 2010;Kang et al., 2019b;Yang et al., 2018). In this section, the trans-boundary
438 transport flux of BC during this severe aerosol pollution event is investigated.
439 According to a previous study, the transport flux can be calculated by projecting the
440 wind field perpendicularly to the cross line and then multiplying the BC mass
441 concentration along the cross line (Zhang et al., 2020). More specifically, the transport
442 flux is calculated as follows:

$$443 \quad \text{TF} = C \cdot (u \cdot \sin \alpha + v \cdot \sin \beta), \quad (1)$$

444 where α is the angle between the east–west wind component and the cross line, β
445 is the angle between the south–north wind component and the cross line, and C is the
446 BC mass concentration at the grid along the cross line. The flux is estimated at each
447 model level. Positive values represent the transport towards the TP, while negative
448 values represent the transport away from the TP. Figure 5 presents the longitude-height
449 cross section of BC transport flux along the cross line (shown as the blue dashed line
450 in Figure 2) from the simulation with aerosol-meteorology feedback at 15:00 and 03:00
451 BJT averaged for the period from April 27 to May 4 (the most polluted period) to
452 represent daytime and nighttime transport, respectively. Notably, BC is imported into
453 the TP in the central and western Himalayas (to the west of $\sim 94^\circ\text{E}$) during the day and
454 night, especially obvious at the height of below 7 km, although the transport flux during
455 the nighttime is much larger than that during the daytime. In the eastern Himalayas
456 (from $94\text{--}98^\circ\text{E}$), BC is imported into the TP during the day but exported slightly from



457 the TP during the night. To the east of $\sim 98^\circ\text{E}$, the BC is transported away from the TP
458 during the day and night due to the prevailed westerly winds. The transport across the
459 western Himalayas is controlled by the large-scale westerly, while the transport across
460 the central and eastern Himalayas is primarily dominated by a local southerly (Zhang
461 et al., 2020). Therefore, the difference in BC transport flux between the western and
462 eastern Himalayas is attributed to the influence of a large-scale westerly that is weak
463 over the eastern Himalayas. The stronger diurnal variation of local southerly (towards
464 the TP in the daytime to away from the TP in the nighttime) compared to that of a
465 westerly near the surface leads to the large difference in diurnal variation of the
466 transport between the western and eastern Himalayas. In addition, the largest BC
467 transport flux along the cross line occurs at deeper mountain valley channels (Figure 5).
468 Zhang et al. (2020) investigated the impact of topography on BC transport to the
469 southern TP during the pre-monsoon season and found that the BC transport across the
470 Himalayas could overcome the majority of mountain ridges, but the valley transport is
471 more efficient, which is consistent with the results obtained in this study.

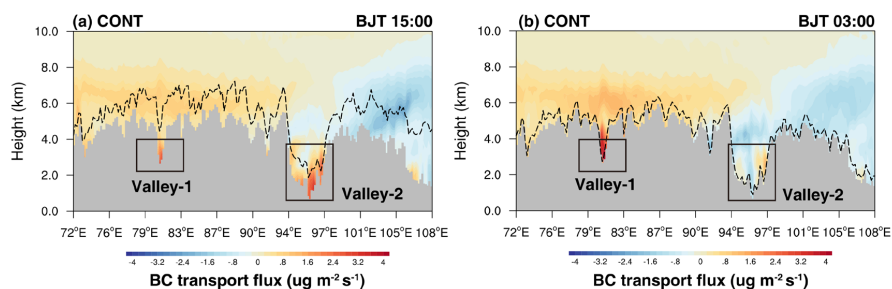
472 As the largest BC transport flux occurs at deeper mountain valleys, the two deepest
473 mountain valley channels along the cross line shown as the blue solid line in Figure 2
474 are selected to demonstrate the transport flux of BC mass across mountain valleys
475 during this severe pollution event. The first valley (referred to as valley-1 hereon) is
476 located in the southwestern TP, while the second valley (referred to as valley-2 hereon)
477 is located in the southeastern TP. It is seen that, at valley-1, the overall positive values
478 near the surface indicate that BC is imported into the TP during the daytime and



479 nighttime, though the transport flux at night is much larger than that during the daytime
480 (Figure 5). Averaged BC concentration and transport flux at 03:00 and 15:00 BJT during
481 the period from April 27 to May 4, 2016 across valley-1 from the simulation with
482 aerosol-meteorology feedback also shows that the BC transport flux is much higher
483 during the night than that during the daytime (Figure 6a–b). By checking the surface
484 BC concentration from simulation with aerosol-meteorology feedback, it is found that
485 the surface BC concentration at valley-1 during the night is much higher than that
486 during the daytime (Table 1). Moreover, the vertically integrated BC concentration over
487 the study area exhibits higher cross-Himalayan transport of BC during the night than
488 that during the daytime (Figure S7), which further provides evidence for the higher BC
489 transport flux during the night shown in Figure 6b. At valley-2, the near-surface positive
490 flux values during the daytime and negative values during the night denote that BC is
491 imported into the TP during the daytime but exported slightly from the TP at night
492 (Figure 5). To analyze this distinct diurnal variation in BC transport flux, we present
493 the latitude–height cross section of BC transport flux and its concentration at 03:00 and
494 15:00 BJT averaged for the period from April 27 to May 4, 2016 across valley-2 from
495 the simulation with aerosol-meteorology feedback as shown in Figure 6c–d. Notably,
496 the deeper PBLH and the strong turbulent mixing during the daytime over northern
497 India allows BC to be mixed at a higher altitude (Figure 6c). Subsequently, the local
498 southerlies boost the BC transporting across the eastern Himalayas towards the TP.
499 Nevertheless, during the night, the meridional wind is dominated by a northerly over
500 the eastern Himalayan region (Figure 6d), which indicates that the cross-Himalayan



501 transport is away from the TP.



502

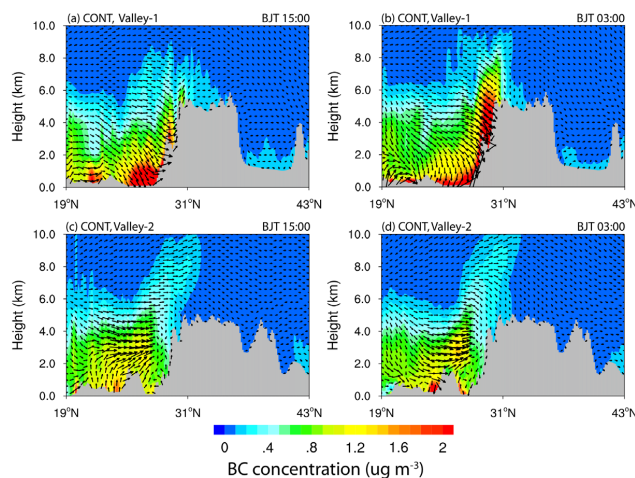
503 Figure 5 Longitude–height cross section of BC transport flux along the cross line

504 (shown as the blue dashed line in Figure 2) at 15:00 and 03:00 BJT averaged for the

505 period from April 27 to May 4, 2016 from simulation with aerosol-meteorology

506 feedback. The PBLH along the cross section is shown here as the black dashed line.

507



508

509 Figure 6 Latitude–height cross section of BC transport flux (vector) across the mountain

510 valley-1 (a, b) and valley-2 (c, d) at 15:00 and 03:00 BJT averaged for the period from

511 April 27 to May 4, 2016 from the simulation with aerosol-meteorology feedback.

512 Contour represents the BC concentration.



513

514 Table 1. Surface BC concentration at two typical mountain valley channels at 15:00 and
 515 03:00 BJT averaged for the period from April 27 to May 4, 2016 from simulation with
 516 aerosol-meteorology feedback.

Near-surface BC concentration	15:00		03:00	
	Valley-1	Valley-2	Valley-1	Valley-2
CONT	1.27	0.75	2.55	0.46

517

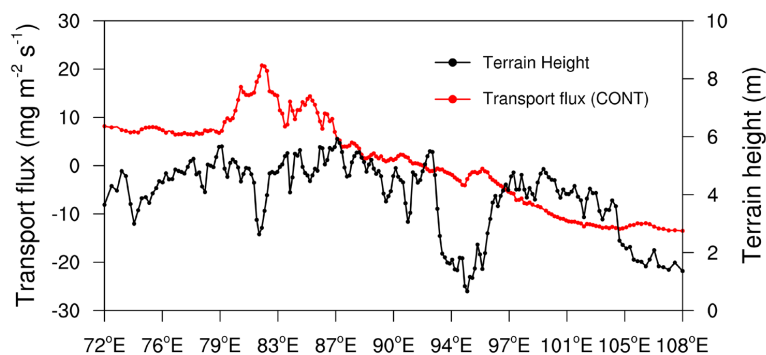
518 To further demonstrate the overall inflow flux across the Himalayas, the vertically
 519 integrated BC mass flux along the longitudinal cross section as shown in Figure 5 from
 520 simulation with aerosol-meteorology feedback is shown in Figure 7. The total mass flux
 521 is calculated by integrating the right-hand term of Eq. (1) as follows:

$$522 \quad ITF = \int_{z=z_{sf}}^{z=z_{top}} \delta z \cdot C \cdot (\mu \cdot \sin\alpha + v \cdot \sin\beta), \quad (2)$$

523 where δz is the thickness of each vertical model level. Similarly, positive flux
 524 values represent the transport towards the TP, while negative values represent the
 525 transport away from the TP. It has been found that the positive values primarily exist in
 526 the central and western Himalayas (to the west of 92 °E), while negative values mainly
 527 exist to the east of 92 °E (Figure 7). Furthermore, the vertically integrated transport flux
 528 of BC along the cross line is strongly correlated with the longitudinal degree of the
 529 cross line, with the correlation coefficient up to -0.89 , passing the 99% confidence level.
 530 This indicates that the vertically integrated transport flux of BC along the cross line
 531 decreases from west to east. In particular, from 80 to 86 °E along the cross line, the



532 correlation coefficient between the terrain height and the vertically integrated transport
533 flux of BC is -0.87 , exceeding the 99% confidence level, suggesting that the lower the
534 valleys are, the higher the vertically integrated transport flux transported across the
535 Himalayas can be. Particularly, the largest vertically integrated transport flux about 20.8
536 $\text{mg m}^{-2} \text{s}^{-1}$ occurs at valley-1. However, to the eastern Himalayas (to the east of $\sim 92^\circ \text{E}$),
537 the BC is overall exported away from the TP and the vertically integrated transport flux
538 with the largest value near to zero occurs at valley-2.



539
540 Figure 7 Longitudinal distribution of vertically integrated BC mass flux (red line) along
541 the cross section in Figure 2 from simulation with aerosol-meteorology feedback. The
542 black line represents the terrain height.

543

544 *3.4 Feedback between aerosol and meteorology*

545 Generally, the severe aerosol pollution event is accompanied by complex feedback
546 between aerosol and meteorology. The analysis above confirms that BC in northern
547 South Asia can be transported to the TP via the cross-Himalayan transport during this
548 severe pollution event. Moreover, compared to the eastern Himalayas, the western
549 Himalayas contributes more BC to the TP and BC from the cross-Himalayan transport



550 mainly concentrated in the southern part of the TP. Therefore, in this section, the
551 feedback between aerosol and meteorology over the western Indo-Gangetic Plain
552 (referred to IGP hereon) and southern TP during this severe pollution event is analyzed.

553 To illustrate the aerosol radiative forcing (ARF) and its impacts on T2, RH2,
554 surface energy, atmospheric stability, wind, and PBLH over the southern TP and IGP
555 regions, the time series of aerosol-induced daily and diurnal changes in meteorological
556 variables (T2, RH2) and surface energy budget (latent heat (LH), sensible heat (SH),
557 shortwave (SW) radiation, longwave (LW) radiation, and net energy flux
558 (LH+LW+SH+SW)) averaged for the southern TP and IGP regions, which is calculated
559 by subtracting the model results of SEN from those of CONT, is shown in Figure 8. It
560 should be noted that the diurnal change is calculated for the period from April 27 to
561 May 4, the most polluted period. As can be seen, daily variation of aerosol-induced
562 area-averaged surface air temperature ranged from -0.1 to 0.1 °C in the southern TP,
563 with a discernable decrease of 0.1 °C appearing on May 2, May 4, and May 6–7 (Figure
564 8a), and from -1.7 to 1.2 °C in the IGP (Figure 8c) during the period from April 20 to
565 May 10. During the most polluted period from April 27 to May 4, aerosol-induced
566 surface air temperature ranged from -0.1 to 0.1 °C in the southern TP (Figure 8a), with
567 a decrease of 0.1 °C on May 2 and May 4, and decreased by 0.5 – 1.7 °C in the IGP
568 (Figure 8c). Daily variation of aerosol-induced area-averaged RH2 displayed a slight
569 change with values ranging from -1.6% to 2.3% over the southern TP (Figure 8a) and
570 exhibited a greater range of about -10.9% – 13.7% in the IGP (Figure 8c) during the
571 period from April 20 to May 10. From April 27 to May 4 with high aerosol

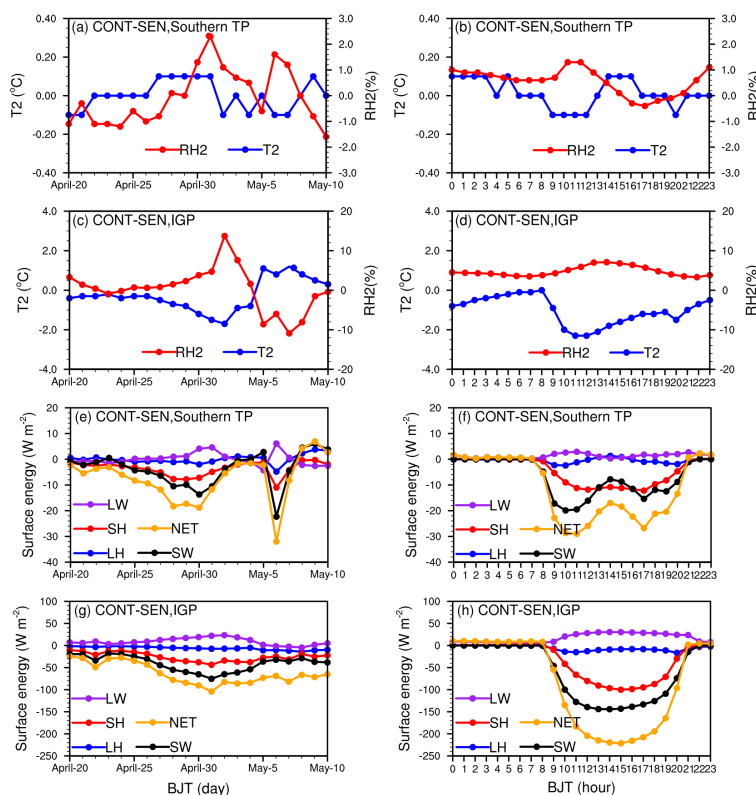


572 concentrations, area-averaged RH2 increased by 0–2.3% and by 0.8%–13.7% in the
573 southern TP and IGP, respectively (Figure 8a, c). For the diurnal change depicted in
574 Figure 8b and Figure 8d, during 09:00–20:00 BJT in the daytime, aerosol-induced area-
575 averaged surface air temperature had a range of about –0.1–0.1 °C in the southern TP
576 and decreased by 0.9–2.3 °C in the IGP. At night, surface air temperature increased by
577 0.1°C during 00:00–05:00 BJT in the southern TP (Figure 8b), and decreased by 0–
578 1.0 °C during 21:00–08:00 BJT in the IGP (Figure 8d). The diurnal change in aerosol-
579 induced RH2 decreased by 0.1%–0.4% during 14:00–17:00 BJT in the southern TP and
580 increased during the rest time of the day, with the maximum increase of 1.3% occurring
581 during 09:00–10:00 BJT (Figure 8b). In the IGP, aerosol-induced RH2 increased by
582 3.3%–7.1% during 09:00–20:00 BJT in the daytime and increased by 2.6%–4.5%
583 during 21:00–08:00 in the nighttime (Figure 8d). Therefore, aerosol-induced changes
584 in T2 and RH2 primarily occur in the daytime.

585 Generally, surface energy with positive values indicates more energy flux toward
586 the surface, and vice versa. Figure 8e–8h present the aerosol-induced surface energy
587 changes over the southern TP and IGP, it is found that the SW radiation flux at the
588 surface decreased by 0–13.7 Wm⁻² in the southern TP (Figure 8e) and by 44.5–75.3
589 Wm⁻² in the IGP (Figure 8g) during the period from April 27 to May 4 due to aerosol
590 scattering and absorption of solar radiation. In contrast, LW radiation flux at the surface
591 of southern TP and IGP increased due to the positive radiative forcing of aerosol in the
592 atmosphere, with an increase of 4.1–4.6 Wm⁻² from April 30 to May 1 in the southern
593 TP (Figure 8e) and a large increase of 12.3–23.4 Wm⁻² from April 27 to May 4 in the



594 IGP (Figure 8g). Because of the cooling effect of aerosols, the LH and SH fluxes from
595 the surface to the atmosphere in both regions decrease. Particularly, in the southern TP,
596 the LH and SH fluxes with the maximum decreases of 2.0 Wm^{-2} and 7.8 Wm^{-2} occurred
597 on April 30 and April 29, respectively (Figure 8e). In the IGP, the LH and SH fluxes
598 decreased by $4.1\text{--}7.4 \text{ Wm}^{-2}$ and by $26.6\text{--}43.6 \text{ Wm}^{-2}$ from April 27 to May 4,
599 respectively (Figure 8g). The net energy flux at the surface decreased by $1.6\text{--}18.8 \text{ W}$
600 m^{-2} in the southern TP (Figure 8e) and by $62.7\text{--}104.3 \text{ Wm}^{-2}$ in the IGP (Figure 8g)
601 from April 27 to May 4. Therefore, the energy arriving at the surface in the southern TP
602 and IGP decrease during this severe aerosol pollution event. For the diurnal change of
603 surface energy, during 09:00–20:00 BJT in the southern TP, the SW, LH, SH, and net
604 energy fluxes decreased by $7.8\text{--}19.9 \text{ Wm}^{-2}$, $0\text{--}2.4 \text{ Wm}^{-2}$, $4.7\text{--}12.2 \text{ Wm}^{-2}$, and $13.4\text{--}29$
605 Wm^{-2} , respectively, while the LW flux increased by $0.3\text{--}2.9 \text{ Wm}^{-2}$ (Figure 8f). During
606 09:00–20:00 BJT in the IGP region, the SW, LH, SH, and net energy fluxes decreased
607 by $46.1\text{--}144.2 \text{ Wm}^{-2}$, $7.5\text{--}16.6 \text{ Wm}^{-2}$, $9.6\text{--}100.1 \text{ Wm}^{-2}$, and $54.7\text{--}221.5 \text{ Wm}^{-2}$,
608 whereas the LW flux increased by $8.5\text{--}30.5 \text{ Wm}^{-2}$ (Figure 8h). Therefore, changes in
609 surface energy mainly occur during the daytime.



610

611 Figure 8 Time series of aerosol-induced daily changes in (a, c) meteorological variables

612 (T2 (°C), RH2 (%)) and (e, g) surface energy budget (SH, LH, LW radiation, SW

613 radiation, and net energy flux, Wm⁻²) averaged for the (a, e) southern TP and (c, g) IGP

614 during the period from April 20 to May 10. Time series of aerosol-induced diurnal

615 changes in (b, d) meteorological variables and (f, h) surface energy budget averaged for

616 the period from April 27 to May 4, 2016 for the (b, f) southern TP and (d, h) IGP. LH

617 is latent heat, LW is long-wave radiation, SH is sensible heat, SW is shortwave radiation,

618 and NET is the sum of the total energy fluxes.

619

620 Figure 9 shows the spatial distribution of aerosol-induced changes in T2 and RH2



621 and aerosol radiative forcing (ARF) at the bottom of atmosphere as well as in the
622 atmosphere, calculated by subtracting the model results of SEN from those of CONT
623 averaged during 09:00–20:00 BJT from April 27 to May 4. As seen in Figure 9a, the
624 aerosol-induced surface air temperature decreased over most parts of the study area
625 except for the TP, where surface air temperature increased, especially obvious in the
626 northern TP, with surface air temperature increasing by up to 1.0 °C. Because the
627 northern TP is proximity to the Taklimakan Desert, where desert dust type aerosols
628 dominate. The strong light absorption of dust aerosols from the Taklimakan Desert
629 increases surface air temperature over the northern TP. Surface air temperature decrease
630 indicates that solar shortwave radiation reaching the surface decreases due to the
631 dimming effect of aerosols. In particular, the largest surface air temperature decrease
632 due to aerosols occurred in South Asia. Because South Asia has large amounts of
633 aerosols due to rapid economic growth, industrialization, and unplanned urbanization
634 compared to other regions (Shi et al., 2020). The spatial distribution of aerosol-induced
635 changes in RH2 is opposite to that of T2, with increased RH2 appearing in most parts
636 of the study area and decreased RH2 on the TP. The largest increase in RH2 occurred
637 in northern South Asia, since the aerosol-induced changes in water vapor mixing ratio
638 is very small, and the decrease in temperature can lead to a decrease in the saturation
639 pressure of water vapor and an increase in RH2 at the surface, which is beneficial for
640 the hygroscopic growth of aerosols (Gao et al., 2015b). By analyzing the time–altitude
641 distribution of the diurnal cycle of aerosol impacts on temperature and relative humidity
642 (RH) averaged for the southern TP and IGP during the period from April 27 to May 4,

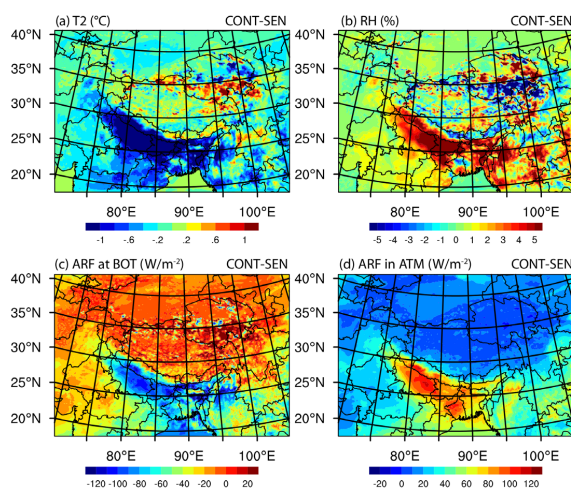


643 it is found that, consistent with aerosol-induced changes in T2 and RH2, the changes in
644 temperature and RH mainly occurred during daytime as well (Figure S8). Specifically,
645 in the southern TP, the maximum increase in temperature with value up to 0.15 °C
646 occurred in the middle troposphere (Figure S8a). However, in the IGP, the temperature
647 decreased near the surface with a maximum drop of more than 0.3 °C and increased in
648 the middle troposphere with a maximum increase of more than 0.3 °C (Figure S8c).
649 There is no doubt that such a temperature change increases the stability of the
650 atmosphere over both regions. Note that the temperature increase in the middle
651 troposphere over the southern TP is more significant than that in the IGP, which is
652 possibly correlated with the thermal pump role of the TP (Li and Yanai, 1996; Meehl,
653 1994; Yanai et al., 1992). The time–altitude distribution of the diurnal cycle of RH is
654 opposite to that of temperature, with RH increasing near the surface and decreasing in
655 the middle troposphere (Figure S8b and Figure S8d). To be exact, RH decreased by 1.6%
656 in the middle troposphere over the southern TP (Figure S8b), while in the IGP, RH
657 increased near the surface with value greater than 3% and decreased by more than 3%
658 in the middle troposphere (Figure S8d).

659 The ARF at the bottom of the atmosphere is negative over most parts of the study
660 area except for the northern TP, where ARF is positive, with ARF up to 20 W m⁻²
661 (Figure 9c). The observed largest negative ARF occurred in northern South Asia and
662 the Bay of Bengal, with values in a range of about -40--120 Wm⁻² (Figure 9c).
663 Contrary to the spatial distribution of ARF at the bottom of the atmosphere, the ARF in
664 the atmosphere is positive over most parts of the study area, with the largest ARF up to



665 110 Wm^{-2} in South Asia (Figure 9d). Thus, affected by aerosols, the atmospheric
666 stratification over the study area is expected to be more stable.



667
668 Figure 9 Spatial distribution of aerosol-induced changes in T2 (°C) (a) and RH2 (%)
669 (b), and aerosol radiative forcing (ARF, Wm^{-2}) at the bottom of (BOT) (c) and in the
670 atmosphere (ATM) (d) averaged for 09:00–20:00 BJT during the period from April 27
671 to May 4, 2016.

672

673 From the above analysis, aerosol-induced changes in meteorological conditions
674 and ARF have significant impact on atmospheric stability. The profile of equivalent
675 potential temperature (EPT) can be used to characterize the stability of the atmosphere.
676 Figure S9 in the SI shows the aerosol-induced changes in EPT profiles at 02:00, 08:00,
677 14:00, and 20:00 BJT, averaged during the period from April 27 to May 4 in the
678 southern TP and IGP. It can be seen that aerosol impact on EPT over the southern TP
679 with values in a range of about 0.08–0.24 K is overall smaller than that in the IGP with
680 values in a range of about -1.6 – 3.2 K due to low aerosol concentrations in the southern

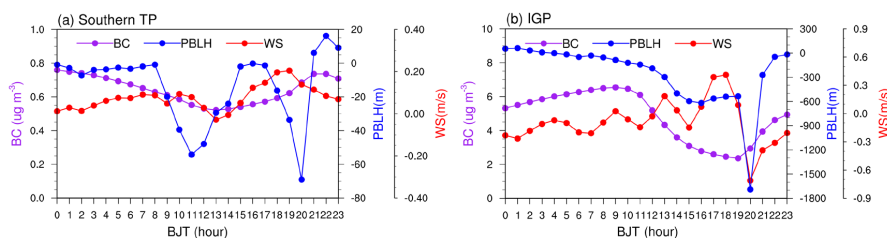


681 TP and high aerosol concentrations in the IGP. Specifically, at 08:00, 14:00 and 20:00
682 BJT, the EPT in the southern TP decreased with height in the lower and middle
683 troposphere, and increased with height above the middle troposphere (Figure S9a).
684 However, in the IGP, at 02:00 and 20:00 BJT, the EPT decreased with height below
685 550 hPa and increased with height above 550 hPa, while at 14:00 BJT, the EPT
686 decreased with height below 650 hPa and increased with height between 650 and 550
687 hPa (Figure S9b). Therefore, an obvious temperature inversion was observed in the
688 troposphere over the southern TP and IGP during the severe aerosol pollution event.

689 Under a more stable atmosphere, the diurnal variation of surface BC
690 concentrations from control experiment with aerosol-meteorology feedback and
691 aerosol-induced changes in U10 and planetary boundary layer height (PBLH) over the
692 southern TP and IGP are presented in Figure 10. Overall, BC concentrations over the
693 southern TP and IGP were high during 20:00–08:00 BJT in the nighttime and low
694 during 08:00–20:00 BJT in the daytime. Over the southern TP, the aerosol-induced
695 PBLH decreased with value up to 55 m during 09:00–14:00 BJT and by 70 m during
696 18:00–20:00 BJT, while at other times of the day, no obvious change in PBLH was
697 observed (Figure 10a). In the IGP, the aerosol-induced PBLH decreased during 10:00–
698 20:00 BJT in the daytime, with the largest decrease of 1700 m occurring at 20:00 BJT
699 (Figure 10b). Lower PBLH constrains the pollutants to diffuse in the vertical direction
700 and is conducive to the accumulation of pollutants near the ground. Aerosol-induced
701 U10 increased in the southern TP, with the maximum increase of 0.2 m/s appearing at
702 19:00 BJT (Figure 10a). In the IGP, the aerosol-induced U10 decreased, with the largest



703 decrease of 0.7 m/s appearing at 20:00 BJT (Figure 10b). Therefore, aerosol induces
 704 significant changes in meteorological conditions in the southern TP and IGP during this
 705 severe aerosol pollution event.



706
 707 Figure 10 Diurnal variation of surface BC concentrations ($\mu\text{g m}^{-3}$) from control
 708 experiment with aerosol-meteorology feedback (purple solid line) and aerosol-induced
 709 diurnal changes in 10-m wind speed (red solid line, WS, m s^{-1}) and PBLH (blue solid
 710 line, m) averaged for (a) the southern TP and (b) IGP during the period from April 27
 711 to May 4, 2016.

712
 713 Aerosol-induced changes in meteorological conditions have important effect on
 714 surface BC concentration, which eventually exerts potential influence on aerosol
 715 pollution as well as weather and climate (Menon et al., 2002). Figure 11a and b show
 716 the hourly surface BC concentration from sensitive experiment without aerosol-
 717 meteorology feedback and the impact of aerosol-induced changes in meteorological
 718 variables on hourly surface BC concentration averaged over the southern TP and IGP
 719 during the period from April 20 to May 10. The corresponding diurnal cycle during the
 720 most polluted period from April 27 to May 4 are shown in Figure 11c and d. The change
 721 in percentage is calculated by comparing with the surface BC concentration from the



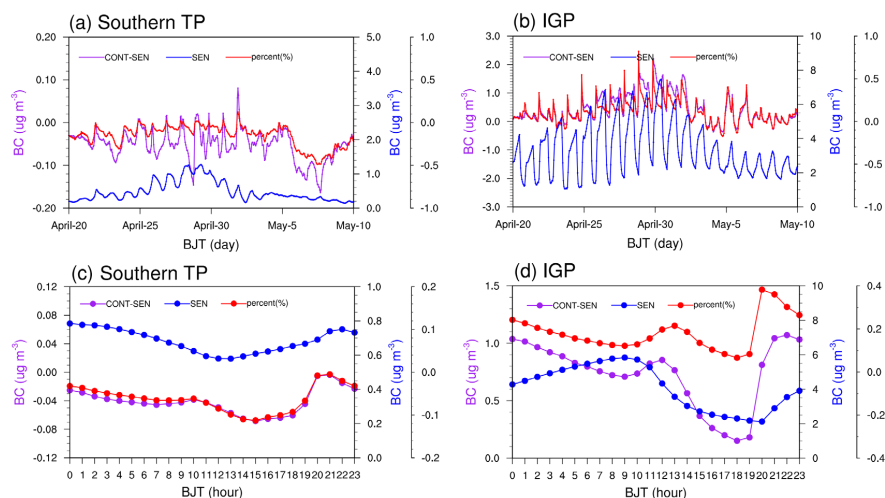
722 experiment without aerosol-meteorology feedback. It can be seen that aerosol-induced
723 changes in meteorological conditions lead to a decrease of surface BC concentration
724 with value up to $0.16 \mu\text{g}/\text{m}^3$ (50%) in the southern TP. However, in the IGP, aerosol-
725 induced changes in meteorological conditions result in an increase in surface BC
726 concentration with value up to $2.2 \mu\text{g}/\text{m}^3$ (75%). Moreover, the higher the surface BC
727 concentration is, the greater the variation in the surface BC concentration induced by
728 meteorological conditions is. It should be noted that the time when the maximum
729 decrease or increase in surface BC concentration occurs is not the time when the
730 maximum surface BC concentration occurs. The diurnal changes in surface BC
731 concentration during the most polluted period from April 27 to May 4 over the southern
732 TP indicate that surface BC concentration is high during 20:00–07:00 BJT in the
733 nighttime and low during 08:00–19:00 BJT in the daytime, with the lowest
734 concentration of $0.6 \mu\text{g}/\text{m}^3$ observed at 12:00 BJT. The changes in meteorological
735 conditions lead to a reduction of surface BC concentration, with the reduction primarily
736 occurring during 11:00–19:00 BJT in the daytime and the largest reduction of 0.06
737 $\mu\text{g}/\text{m}^3$ (12%) appearing at 15:00 BJT. The corresponding diurnal changes in the IGP
738 reveal that surface BC concentration is high during 23:00–12:00 BJT and low during
739 13:00–22:00 BJT. The changes in meteorological conditions result in an increase in
740 surface BC concentration, with the relatively larger increase of about 0.7 – $1.1 \mu\text{g}/\text{m}^3$
741 occurring during 20:00–13:00 BJT. Therefore, the changes in meteorological
742 conditions enhance the diurnal variation of surface BC concentration by decreasing the
743 surface BC concentration in the southern TP and increasing the surface BC



744 concentration in the IGP.

745 Figure S10 in the SI shows the impact of aerosol-induced changes in
746 meteorological conditions on the spatial distribution of surface BC concentration
747 averaged during 09:00–20:00 BJT, April 27–May 4. Consistent with Figure 11, the
748 maximum increase in surface BC concentration induced by changes in meteorological
749 conditions is in the IGP (northwestern South Asia), with values greater than $1 \mu\text{g}/\text{m}^3$.
750 The corresponding surface BC concentration change in percentage terms is also higher
751 in northwestern South Asia with value up to 30%, and is lower in the southeastern TP
752 with value below 30% (Figure S10b). Taken together, aerosols result in significant
753 changes in meteorological conditions in the Southern TP and IGP, with an obvious
754 decrease in PBLH and U10 along with a more stable atmosphere in the IGP, and a
755 decrease in PBLH but an increase in U10 accompanied by a stable atmosphere in the
756 Southern TP. In addition, aerosol-induced changes in meteorological conditions have
757 substantial influence on aerosol concentrations. For instance, in the IGP, changes in
758 meteorological conditions induced by aerosols are conducive to the accumulation of air
759 pollutants, thereby contributing to the formation of severe aerosol pollution event.
760 Consequently, a mechanism of positive feedback exists between aerosol concentration
761 and aerosol-induced meteorological conditions in the IGP. However, as one of the
762 major source regions of air pollutants over the TP, aerosol-induced changes in
763 meteorological conditions in the IGP are not favorable for air pollutants transporting to
764 the southern TP.

765



766

767 Figure 11 Time series of hourly surface BC concentration from SEN (blue solid line)

768 averaged for the southern TP (a) and IGP (b) during the period from April 20 to May

769 10, 2016 and the corresponding diurnal changes (blue solid line) averaged for the

770 southern TP (c) and IGP (d) during the period from April 27 to May 4, 2016. The purple

771 solid line denotes the change value of surface BC concentration induced by

772 meteorological conditions. The red solid line indicates the corresponding change in

773 percentage terms compared to the surface BC concentration from the model results of

774 SEN.

775

776 *3.5 Impact of aerosol-meteorology feedback on the trans-boundary transport flux of*

777 *BC*

778 As discussed above, during the severe aerosol pollution event, northwestern South

779 Asia contributes more BC to the TP via cross-Himalayan transport and the largest BC

780 transport flux occurs at mountain valley in western Himalayas. Moreover, the aerosol-

781 meteorology feedback has a substantial effect on surface BC concentration over the

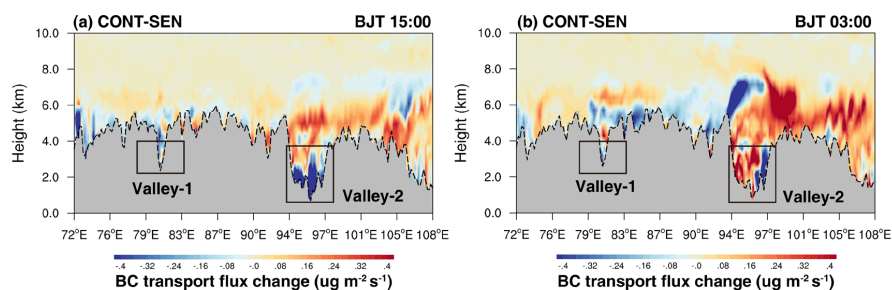


782 southern TP and IGP. Yet what effect the aerosol-meteorology feedback having on the
783 trans-boundary transport flux of BC remains unclear, which deserves further
784 investigation. Therefore, this section is aimed at demonstrating the impact of aerosol-
785 meteorology feedback on the trans-boundary transport flux of BC during the severe
786 aerosol pollution event. Figure 12 shows the difference in longitude–height cross
787 section of BC transport flux along the cross line (shown as the blue dashed line in Figure
788 2) from the simulations with and without aerosol-meteorology feedback at 15:00 and
789 03:00 BJT averaged for the period from April 27 to May 4, 2016. It can be seen that, in
790 the central and western Himalayas (75–90 °E), the aerosol-meteorology feedback
791 during the daytime overall increases the BC transport flux towards the TP at the height
792 of about 6–7 km but decreases the BC transport flux at the height of below 6 km;
793 however, in the eastern Himalayas (90–98 °E), the aerosol-meteorology feedback
794 decreases the BC transport flux exporting from the TP. During the nighttime, the
795 aerosol-meteorology feedback increases the BC transport flux towards the TP at the
796 height of about 6–7 km but decreases the BC transport flux at the height of below 6 km
797 in the central and eastern Himalayas (from 80 °E to 94 °E); however, from 94 °E to
798 98 °E in the eastern Himalayas, the aerosol-meteorology feedback decreases the BC
799 transport flux exporting from the TP.

800 In particular, the impact of aerosol-meteorology feedback on the BC transport flux
801 at two typical mountain valley channels reveals that, at valley-1, the feedback decreases
802 the import of BC towards the TP during the daytime and nighttime; while at valley-2,
803 the feedback decreases the import of BC towards the TP during the daytime and reduces



804 the BC transport flux away from the TP during the nighttime. To better understand the
805 effect of aerosol-meteorology feedback on the BC transport flux at valley-1 and valley-
806 2, we investigated the mean zonal and meridional wind speeds within 3500 m above
807 the ground level at both valleys during the daytime and nighttime from April 27 to May
808 4, 2016 (Table 2) from simulations with and without aerosol-meteorology feedback. It
809 is found that, during the daytime, a westerly and a southerly prevail at valley-1 but an
810 easterly and a southerly prevail at valley-2; during the night, an easterly and a northerly
811 prevail at both valleys in both experiments. Specifically, at valley-1, the differences in
812 zonal and meridional wind speeds between the simulations with and without aerosol-
813 meteorology feedback at 15:00 and 03:00 BJT averaged for the period from April 27 to
814 May 4, 2016 show that, during the daytime, the aerosol-meteorology feedback overall
815 decreases the westerly and southerly wind speeds, resulting in decreased transport flux
816 of BC mass towards the TP; during the night, the aerosol-meteorology feedback leads
817 to increased easterly and northerly wind speeds, which strengthen the BC transport flux
818 away from the TP. The corresponding results at valley-2 indicate that, during the
819 daytime, the aerosol-meteorology feedback increases the easterly wind speed but
820 decreases the southerly wind speed, resulting in decreased transport flux of BC towards
821 the TP; during the night, the aerosol-meteorology feedback increases the easterly wind
822 speed but decreases the northerly wind speed, leading to reduced BC transport flux
823 away from the TP. It is to be emphasized that the results averaged within 3900 m above
824 the ground level (Table S3) are consistent with those averaged within 3500 m.



825

826 Figure 12 Difference in longitude–height cross section of BC transport flux along the
 827 cross line (shown as the blue dashed line in Figure 2) from the simulations with and
 828 without aerosol-meteorology feedback at 15:00 and 03:00 BJT averaged for the period
 829 from April 27 to May 4, 2016. The difference in PBLH along the cross section is shown
 830 here as the black dashed line.

831

832 Table 2. The mean zonal and meridional wind speeds at two typical valley channels
 833 within 3500 m above the ground level at 15:00 and 03:00 BJT averaged for the period
 834 from April 27 to May 4, 2016 between the CONT and SEN experiments. The
 835 differences in zonal and meridional wind speeds between the two experiments are also
 836 shown. Positive value denotes a westerly or a southerly and negative value denotes an
 837 easterly or a northerly.

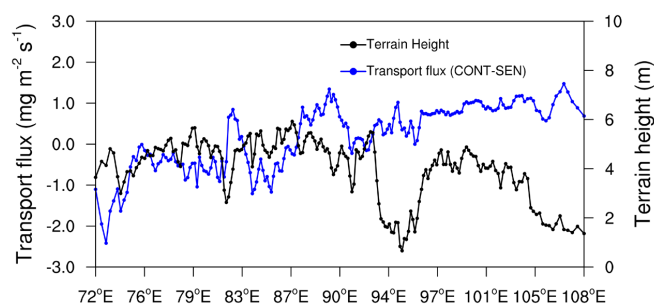
3500 m		15:00		03:00	
		Valley-1	Valley-2	Valley-1	Valley-2
CONT	U component	2.32	-1.90	-1.34	-1.19
	V component	4.74	1.35	-1.73	-1.56
SEN	U component	2.75	-1.43	-1.26	-1.07
	V component	4.94	1.61	-1.60	-1.92
CONT-SEN	U component	-0.43	-0.47	-0.08	-0.12
	V component	-0.2	-0.26	-0.13	0.36

838

839 Similarly, the impact of aerosol-meteorology feedback on the vertically integrated



840 trans-boundary transport flux of BC along the cross line shown as the blue dashed line
841 in Figure 2 reveals that, with the aerosol-meteorology feedback, the integrated transport
842 flux of BC mass from central and western Himalayas (to the west of 88 °E) to the TP
843 overall decreases; however, in the eastern Himalayas, the aerosol-meteorology
844 feedback increases the integrated transport flux of BC towards the TP (Figure 13).
845 Therefore, aerosol-meteorology feedback exerts a very important effect on trans-
846 boundary transport flux of BC.



847

848 Figure 13 Difference in longitudinal distribution of integrated BC mass flux along the
849 cross section in Figure 2 from the simulations with and without aerosol-meteorology
850 feedback. The black line represents the terrain height.

851

852 4 Conclusion

853 The worst aerosol pollution episode ever recorded over the TP occurred during the
854 period from April 20 to May 10, 2016. The observed largest AOD at reference sites of
855 Nam Co and QOMS are 0.65 and 0.42, respectively. In this paper, the meteorological
856 causes, BC transport flux, and aerosol-meteorology feedback as well as its effect on BC
857 transport flux during this severe aerosol pollution event are investigated by using



858 observational and reanalysis dataset, and numerical simulation from WRF-Chem. By
859 analyzing the evolution of weather maps at 500 hPa over the study area during this
860 severe aerosol pollution event, it is found that the plateau vortex plays a critical role in
861 increasing aerosol concentrations in the inland of the TP. However, in the southern TP,
862 the increase in aerosol concentration could be attributed to the long-range transport by
863 southwesterly airflow in front of the trough.

864 With the acceptable performance of WRF-Chem model on simulating
865 meteorological conditions and aerosols, we estimated the trans-boundary transport flux
866 of BC across the Himalayas. The results show that, in the central and western
867 Himalayas, BC is imported into the TP during the day and night; in the eastern
868 Himalayas, BC is imported into the TP during the day but exported slightly from the
869 TP during the night; however, to the east of $\sim 98^\circ\text{E}$, BC is transported away from the
870 TP during the day and night. The vertically integrated transport flux of BC along the
871 cross line during the aerosol pollution event decreases from west to east. The largest
872 vertically integrated transport flux of BC with value up to $20.8 \text{ mg m}^{-2} \text{ s}^{-1}$ occurs at a
873 mountain valley in southwestern TP.

874 By designing experiments with or without aerosol-meteorology feedback, the
875 feedback between aerosol and meteorology over the southern TP and IGP during this
876 severe aerosol pollution event are investigated. It has been found that during the most
877 polluted period from April 27 to May 4, aerosols lead to a slight change in surface air
878 temperature in the southern TP but a significant decrease by $0.5\text{--}1.7^\circ\text{C}$ in the IGP.
879 Vertically, in the southern TP, the largest temperature increase induced by aerosols



880 occurs in the middle troposphere; however, in the IGP, aerosol-induced temperature
881 decreases near the surface but increases in the middle troposphere. Spatially, the ARF
882 is negative at the bottom of the atmosphere but is positive in the atmosphere over most
883 parts of the study area. As a result, the atmospheric stratification over the study area is
884 more stable. Additionally, affected by aerosols, U10 increases in the southern TP, with
885 the largest increase of 0.2 m/s appearing at 19:00 BJT; while in the IGP, U10 decreases,
886 with the largest decrease of 0.7 m/s appearing at 20:00 BJT. In respect to PBLH,
887 aerosols lead to a decrease by 55 m in PBLH during 09:00–14:00 BJT and by 60 m
888 during 17:00–20:00 BJT in the southern TP; whereas in the IGP, a decrease in PBLH
889 resulted from aerosols mainly occurs during 10:00–20:00 BJT in the daytime, with the
890 largest decrease of 1300 m detected at 20:00 BJT. Therefore, aerosols exert an
891 important effect on meteorological conditions. By contrast, aerosol-induced changes in
892 meteorological conditions can lead to a decrease of surface BC concentration with value
893 up to 0.16 $\mu\text{g}/\text{m}^3$ (50%) in the southern TP and an increase of surface BC concentration
894 with value up to 2.2 $\mu\text{g}/\text{m}^3$ (75%) in the IGP.

895 By investigating the impact of aerosol-meteorology feedback on the BC transport
896 flux, it has been acquired that, with the aerosol-meteorology feedback, the integrated
897 transport flux of BC mass from central and western Himalayas to the TP overall
898 decreases; however, in the eastern Himalayas, the aerosol-meteorology feedback
899 increases the integrated transport flux of BC towards the TP. In particular, the
900 corresponding results at two typical mountain valley channels in southwestern and
901 southeastern TP reveal that the aerosol-meteorology feedback decreases the import of



902 BC towards the TP at mountain valley channel in southwestern TP during the daytime
903 and nighttime, while at mountain valley channel in the southeastern TP, the feedback
904 decreases the import of BC towards the TP during the daytime and reduces the BC
905 transport flux away from the TP during the nighttime.

906 There are still uncertainties in this study. Because the aerosol feedback derived
907 from the aerosol radiative effect mainly has large impacts during the daytime. From the
908 statistical analysis of model performance on aerosols, we find that the model overall
909 underestimates the AOD. This underestimation may have important effect on aerosol
910 feedback during the most polluted period. Moreover, the feedback between aerosol and
911 meteorological conditions also has uncertainty due to the fact that the aerosol direct and
912 indirect effect is very sensitive to the mixing state between scattering aerosols and
913 absorbing aerosols. In addition, the BC transport flux quantified by WRF-Chem model
914 has bias to some extent. However, with the scarce observation over the TP, numerical
915 model is the best tool for this study. Therefore, emissions with higher resolution and
916 finer model horizontal resolution could improve model performance, since further in-
917 depth investigation is deserved.

918 **Data availability**

919 All raw data can be provided by the corresponding authors upon request.

920 **Author contributions**

921 Shichang Kang and Haipeng Yu provided idea for this paper. Yuling Hu and
922 Junhua Yang designed the experiments and performed the simulations. Yuling Hu wrote
923 the code and explained the model results. Pengfei Chen provided the data to verify the



924 model results. Yuling Hu, Mukesh Rai, Xiufeng Yin, and Xintong Chen prepared,
925 reviewed and edited the manuscript with contributions from all co-authors.

926 **Competing interests**

927 The authors declare that they have no conflict of interest.

928 **Acknowledgments**

929 This study was supported by the National Natural Science Foundation of China
930 (42205123), the Chinese Academy of Sciences (XDA20040501, QYZDJ-SSW-
931 DQC039), and the State Key Laboratory of Cryospheric Science (SKLCS-ZZ-2023).
932 The authors would like to acknowledge the National Centers for Environmental
933 Prediction (NCEP) and the European Centre for Medium-Range Weather Forecasts
934 (ECMWF) for providing final analysis data and reanalysis data, respectively.

935 **References**

- 936 Bran, S. H., and Srivastava, R.: Investigation of PM_{2.5} mass concentration over India using a regional
937 climate model, *Environmental Pollution*, 224, 484-493. <https://doi.org/10.1016/j.envpol.2017.02.030>,
938 2017.
- 939 Buchard, V., Randles, C. A., da Silva, A. M., Darmenov, A., Colarco, P. R., Govindaraju, R., Ferrare, R., Hair,
940 J., Beyersdorf, A. J., Ziemba, L. D., and Yu, H.: The MERRA-2 Aerosol Reanalysis, 1980 Onward. Part II:
941 Evaluation and Case Studies, *Journal of Climate*, 30, 6851-6872. [https://doi.org/10.1175/JCLI-D-16-
942 0613.1](https://doi.org/10.1175/JCLI-D-16-0613.1), 2017.
- 943 Che, H., Gui, K., Xia, X., Wang, Y., Holben, B. N., Goloub, P., Cuevas-Agulló, E., Wang, H., Zheng, Y., Zhao,
944 H., and Zhang, X.: Large contribution of meteorological factors to inter-decadal changes in regional
945 aerosol optical depth, *Atmos. Chem. Phys.*, 19, 10497-10523. [https://doi.org/10.5194/acp-19-10497-
946 2019](https://doi.org/10.5194/acp-19-10497-2019), 2019.
- 947 Chen, L., Zhu, J., Liao, H., Gao, Y., Qiu, Y. L., Zhang, M. G., Liu, Z. R., Li, N., and Wang, Y. S.: Assessing the
948 formation and evolution mechanisms of severe haze pollution in the Beijing-Tianjin-Hebei region using
949 process analysis, *ATMOSPHERIC CHEMISTRY AND PHYSICS*, 19, 10845-10864.
950 <https://doi.org/10.5194/acp-19-10845-2019>, 2019a.
- 951 Chen, X., Kang, S., Cong, Z., Yang, J., and Ma, Y.: Concentration, temporal variation, and sources of black
952 carbon in the Mt. Everest region retrieved by real-time observation and simulation, *Atmos. Chem. Phys.*,
953 18, 12859-12875. <https://doi.org/10.5194/acp-18-12859-2018>, 2018.
- 954 Chen, Y., Yang, K., Zhou, D., Qin, J., and Guo, X.: Improving the Noah Land Surface Model in Arid Regions
955 with an Appropriate Parameterization of the Thermal Roughness Length, *Journal of Hydrometeorology*,



- 956 11, 995-1006. <https://doi.org/10.1175/2010JHM1185.1>, 2010.
- 957 Chen, Y., Zhou, Y., and Zhao, X.: PM_{2.5} over North China based on MODIS AOD and effect of
958 meteorological elements during 2003–2015, *Frontiers of Environmental Science & Engineering*, 14, 23.
959 <https://doi.org/10.1007/s11783-019-1202-8>, 2019b.
- 960 Chin, M., Ginoux, P., Kinne, S., Torres, O., Holben, B. N., Duncan, B. N., Martin, R. V., Logan, J. A., Higurashi,
961 A., and Nakajima, T.: Tropospheric Aerosol Optical Thickness from the GOCART Model and Comparisons
962 with Satellite and Sun Photometer Measurements, *Journal of the Atmospheric Sciences*, 59, 461-483.
963 [https://doi.org/10.1175/1520-0469\(2002\)059<0461:TAOTFT>2.0.CO;2](https://doi.org/10.1175/1520-0469(2002)059<0461:TAOTFT>2.0.CO;2), 2002.
- 964 China, S., Scarnato, B., Owen, R. C., Zhang, B., Ampadu, M. T., Kumar, S., Dzepina, K., Dziobak, M. P.,
965 Fialho, P., Perlinger, J. A., Hueber, J., Helmig, D., Mazzoleni, L. R., and Mazzoleni, C.: Morphology and
966 mixing state of aged soot particles at a remote marine free troposphere site: Implications for optical
967 properties, *Geophysical Research Letters*, 42, 1243-1250. <https://doi.org/10.1002/2014GL062404>,
968 2015.
- 969 Chung, C. E., Ramanathan, V., Kim, D., and Podgorny, I. A.: Global anthropogenic aerosol direct forcing
970 derived from satellite and ground-based observations, *Journal of Geophysical Research: Atmospheres*,
971 110. <https://doi.org/10.1029/2005JD006356>, 2005.
- 972 Chung, C. E., Cha, H., Vihma, T., Räisänen, P., and Decremier, D.: On the possibilities to use atmospheric
973 reanalyses to evaluate the warming structure in the Arctic, *Atmos. Chem. Phys.*, 13, 11209-11219.
974 <https://doi.org/10.5194/acp-13-11209-2013>, 2013.
- 975 Colarco, P., da Silva, A., Chin, M., and Diehl, T.: Online simulations of global aerosol distributions in the
976 NASA GEOS-4 model and comparisons to satellite and ground-based aerosol optical depth, *Journal of*
977 *Geophysical Research: Atmospheres*, 115. <https://doi.org/10.1029/2009JD012820>, 2010.
- 978 Duan, A., Wu, G., Zhang, Q., and Liu, Y.: New proofs of the recent climate warming over the Tibetan
979 Plateau as a result of the increasing greenhouse gases emissions, *Chinese Science Bulletin*, 51, 1396-
980 1400. <https://doi.org/10.1007/s11434-006-1396-6>, 2006.
- 981 Dubovik, O., and King, M. D.: A flexible inversion algorithm for retrieval of aerosol optical properties
982 from Sun and sky radiance measurements, *Journal of Geophysical Research: Atmospheres*, 105, 20673-
983 20696. <https://doi.org/10.1029/2000JD900282>, 2000.
- 984 Ek, M. B., Mitchell, K. E., Lin, Y., Rogers, E., Grunmann, P., Koren, V., Gayno, G., and Tarpley, J. D.:
985 Implementation of Noah land surface model advances in the National Centers for Environmental
986 Prediction operational mesoscale Eta model, *Journal of Geophysical Research: Atmospheres*, 108.
987 <https://doi.org/10.1029/2002JD003296>, 2003.
- 988 Fast, J. D., Gustafson Jr, W. I., Easter, R. C., Zaveri, R. A., Barnard, J. C., Chapman, E. G., Grell, G. A., and
989 Peckham, S. E.: Evolution of ozone, particulates, and aerosol direct radiative forcing in the vicinity of
990 Houston using a fully coupled meteorology-chemistry-aerosol model, *Journal of Geophysical Research:*
991 *Atmospheres*, 111. <https://doi.org/10.1029/2005JD006721>, 2006.
- 992 Flanner, M. G., Zender, C. S., Randerson, J. T., and Rasch, P. J.: Present-day climate forcing and response
993 from black carbon in snow, *Journal of Geophysical Research: Atmospheres*, 112.
994 <https://doi.org/10.1029/2006JD008003>, 2007.
- 995 Gao, M., Carmichael, G. R., Wang, Y., Saide, P. E., and Wang, Z.: Modeling study of the 2010 regional
996 haze event in the North China Plain, *Atmospheric Chemistry & Physics*, 15, 2015a.
- 997 Gao, Y., Zhang, M., Liu, Z., Wang, L., Wang, P., Xia, X., Tao, M., and Zhu, L.: Modeling the feedback
998 between aerosol and meteorological variables in the atmospheric boundary layer during a severe fog-
999 haze event over the North China Plain, *Atmos. Chem. Phys.*, 15, 4279-4295.



- 1000 <https://doi.org/10.5194/acp-15-4279-2015>, 2015b.
- 1001 Gelaro, R., McCarty, W., Suárez, M. J., Todling, R., Molod, A., Takacs, L., Randles, C. A., Darmenov, A.,
1002 Bosilovich, M. G., Reichle, R., Wargan, K., Coy, L., Cullather, R., Draper, C., Akella, S., Buchard, V., Conaty,
1003 A., da Silva, A. M., Gu, W., Kim, G.-K., Koster, R., Lucchesi, R., Merkova, D., Nielsen, J. E., Partyka, G.,
1004 Pawson, S., Putman, W., Rienecker, M., Schubert, S. D., Sienkiewicz, M., and Zhao, B.: The Modern-Era
1005 Retrospective Analysis for Research and Applications, Version 2 (MERRA-2), *Journal of Climate*, 30, 5419-
1006 5454. <https://doi.org/10.1175/JCLI-D-16-0758.1>, 2017.
- 1007 Grell, G. A., Peckham, S. E., Schmitz, R., McKeen, S. A., Frost, G., Skamarock, W. C., and Eder, B.: Fully
1008 coupled “online” chemistry within the WRF model, *Atmospheric Environment*, 39, 6957-6975.
1009 <https://doi.org/10.1016/j.atmosenv.2005.04.027>, 2005.
- 1010 Grell, G. A., and Freitas, S. R.: A scale and aerosol aware stochastic convective parameterization for
1011 weather and air quality modeling, *Atmos. Chem. Phys.*, 14, 5233-5250. <https://doi.org/10.5194/acp-14-5233-2014>, 2014.
- 1013 Guenther, A., Karl, T., Harley, P., Wiedinmyer, C., Palmer, P. I., and Geron, C.: Estimates of global
1014 terrestrial isoprene emissions using MEGAN (Model of Emissions of Gases and Aerosols from Nature),
1015 *Atmos. Chem. Phys.*, 6, 3181-3210. <https://doi.org/10.5194/acp-6-3181-2006>, 2006.
- 1016 Guenther, A. B., Jiang, X., Heald, C. L., Sakulyanontvittaya, T., Duhl, T., Emmons, L. K., and Wang, X.: The
1017 Model of Emissions of Gases and Aerosols from Nature version 2.1 (MEGAN2.1): an extended and
1018 updated framework for modeling biogenic emissions, *Geosci. Model Dev.*, 5, 1471-1492.
1019 <https://doi.org/10.5194/gmd-5-1471-2012>, 2012.
- 1020 Hansen, J., and Nazarenko, L.: Soot climate forcing via snow and ice albedos, *Proceedings of the National*
1021 *Academy of Sciences of the United States of America*, 101, 423.
1022 <https://doi.org/10.1073/pnas.2237157100>, 2004.
- 1023 He, C., Liou, K. N., Takano, Y., Zhang, R., Levy Zamora, M., Yang, P., Li, Q., and Leung, L. R.: Variation of
1024 the radiative properties during black carbon aging: theoretical and experimental intercomparison,
1025 *Atmos. Chem. Phys.*, 15, 11967-11980. <https://doi.org/10.5194/acp-15-11967-2015>, 2015.
- 1026 Heidinger, A. K., Foster, M. J., Walther, A., and Zhao, X.: The Pathfinder Atmospheres–Extended AVHRR
1027 Climate Dataset, *Bulletin of the American Meteorological Society*, 95, 909-922.
1028 <https://doi.org/10.1175/BAMS-D-12-00246.1>, 2014.
- 1029 Holben, B. N., Eck, T. F., Slutsker, I., Tanré, D., Buis, J. P., Setzer, A., Vermote, E., Reagan, J. A., Kaufman,
1030 Y. J., Nakajima, T., Lavenu, F., Jankowiak, I., and Smirnov, A.: AERONET—A Federated Instrument Network
1031 and Data Archive for Aerosol Characterization, *Remote Sensing of Environment*, 66, 1-16.
1032 [https://doi.org/10.1016/S0034-4257\(98\)00031-5](https://doi.org/10.1016/S0034-4257(98)00031-5), 1998.
- 1033 Hong, C. P., Zhang, Q., Zhang, Y., Davis, S. J., Zhang, X., Tong, D., Guan, D. B., Liu, Z., and He, K. B.:
1034 Weakening aerosol direct radiative effects mitigate climate penalty on Chinese air quality, *NATURE*
1035 *CLIMATE CHANGE*, 10, 845-+. <https://doi.org/10.1038/s41558-020-0840-y>, 2020.
- 1036 Hsu, N. C., Jeong, M. J., Bettenhausen, C., Sayer, A. M., Hansell, R., Seftor, C. S., Huang, J., and Tsay, S. C.:
1037 Enhanced Deep Blue aerosol retrieval algorithm: The second generation, *Journal of Geophysical*
1038 *Research: Atmospheres*, 118, 9296-9315. <https://doi.org/10.1002/jgrd.50712>, 2013.
- 1039 Hu, Y., Kang, S., Yang, J., Chen, X., Ji, Z., and Rai, M.: Transport of black carbon from Central and West
1040 Asia to the Tibetan Plateau: Seasonality and climate effect, *Atmospheric Research*, 267, 105987.
1041 <https://doi.org/10.1016/j.atmosres.2021.105987>, 2022.
- 1042 Iacono, M. J., Delamere, J. S., Mlawer, E. J., Shephard, M. W., Clough, S. A., and Collins, W. D.: Radiative
1043 forcing by long-lived greenhouse gases: Calculations with the AER radiative transfer models, *Journal of*



- 1044 Geophysical Research: Atmospheres, 113. <https://doi.org/10.1029/2008JD009944>, 2008.
- 1045 Janjić, Z. I.: The Step-Mountain Eta Coordinate Model: Further Developments of the Convection, Viscous
1046 Sublayer, and Turbulence Closure Schemes, *Monthly Weather Review*, 122, 927-945.
1047 [https://doi.org/10.1175/1520-0493\(1994\)122<0927:TSMECM>2.0.CO;2](https://doi.org/10.1175/1520-0493(1994)122<0927:TSMECM>2.0.CO;2), 1994.
- 1048 Janssens-Maenhout, G., Crippa, M., Guizzardi, D., Dentener, F., Muntean, M., Pouliot, G., Keating, T.,
1049 Zhang, Q., Kurokawa, J., Wankmüller, R., Denier van der Gon, H., Kuenen, J. J. P., Klimont, Z., Frost, G.,
1050 Darras, S., Koffi, B., and Li, M.: HTAP_v2.2: a mosaic of regional and global emission grid maps for 2008
1051 and 2010 to study hemispheric transport of air pollution, *Atmos. Chem. Phys.*, 15, 11411-11432.
1052 <https://doi.org/10.5194/acp-15-11411-2015>, 2015.
- 1053 Ji, Z., Kang, S., Zhang, D., Zhu, C., Wu, J., and Xu, Y.: Simulation of the anthropogenic aerosols over South
1054 Asia and their effects on Indian summer monsoon, *Climate dynamics*, 36, 1633-1647. 2011.
- 1055 Kahn, R. A., Gaitley, B. J., Martonchik, J. V., Diner, D. J., Crean, K. A., and Holben, B.: Multiangle Imaging
1056 Spectroradiometer (MISR) global aerosol optical depth validation based on 2 years of coincident Aerosol
1057 Robotic Network (AERONET) observations, *Journal of Geophysical Research: Atmospheres*, 110.
1058 <https://doi.org/10.1029/2004JD004706>, 2005.
- 1059 Kang, S., Xu, Y., You, Q., Flügel, W.-A., Pepin, N., and Yao, T.: Review of climate and cryospheric change
1060 in the Tibetan Plateau, *Environmental Research Letters*, 5, 015101. <https://doi.org/10.1088/1748-9326/5/1/015101>, 2010.
- 1062 Kang, S., Cong, Z., Wang, X., Zhang, Q., Ji, Z., Zhang, Y., and Xu, B.: The transboundary transport of air
1063 pollutants and their environmental impacts on Tibetan Plateau, *Chinese Science Bulletin*, 64, 2876-2884.
1064 2019a.
- 1065 Kang, S., Zhang, Q., Qian, Y., Ji, Z., Li, C., Cong, Z., Zhang, Y., Guo, J., Du, W., Huang, J., You, Q., Panday, A.
1066 K., Rupakheti, M., Chen, D., Gustafsson, Ö., Thiemens, M. H., and Qin, D.: Linking atmospheric pollution
1067 to cryospheric change in the Third Pole region: current progress and future prospects, *National Science*
1068 *Review*, 6, 796-809. <https://doi.org/10.1093/nsr/nwz031>, 2019b.
- 1069 Lau, K., Kim, M., and Kim, K.: Asian summer monsoon anomalies induced by aerosol direct forcing: the
1070 role of the Tibetan Plateau, *Climate dynamics*, 26, 855-864. [https://doi.org/10.1007/s00382-006-0114-](https://doi.org/10.1007/s00382-006-0114-z)
1071 [z](https://doi.org/10.1007/s00382-006-0114-z), 2006.
- 1072 Lelieveld, J., Crutzen, P. J., Ramanathan, V., Andreae, M. O., Brenninkmeijer, C. A. M., Campos, T., Cass,
1073 G. R., Dickerson, R. R., Fischer, H., de Gouw, J. A., Hansel, A., Jefferson, A., Kley, D., de Laat, A. T. J., Lal,
1074 S., Lawrence, M. G., Lobert, J. M., Mayol-Bracero, O., Mitra, A. P., Novakov, T., Oltmans, S. J., Prather, K.
1075 A., Reiner, T., Rodhe, H., Scheeren, H. A., Sikka, D., and Williams, J.: The Indian Ocean Experiment:
1076 Widespread Air Pollution from South and Southeast Asia, in: Paul J. Crutzen: A Pioneer on Atmospheric
1077 Chemistry and Climate Change in the Anthropocene, edited by: Crutzen, P. J., and Brauch, H. G., Springer
1078 International Publishing, Cham, 197-209, 2016.
- 1079 Levy, R. C., Remer, L. A., Kleidman, R. G., Mattoo, S., Ichoku, C., Kahn, R., and Eck, T. F.: Global evaluation
1080 of the Collection 5 MODIS dark-target aerosol products over land, *Atmos. Chem. Phys.*, 10, 10399-10420.
1081 <https://doi.org/10.5194/acp-10-10399-2010>, 2010.
- 1082 Li, C., and Yanai, M.: The Onset and Interannual Variability of the Asian Summer Monsoon in Relation to
1083 Land–Sea Thermal Contrast, *Journal of Climate*, 9, 358-375. [https://doi.org/10.1175/1520-0442\(1996\)009<0358:TOAIVO>2.0.CO;2](https://doi.org/10.1175/1520-0442(1996)009<0358:TOAIVO>2.0.CO;2), 1996.
- 1085 Li, C., Bosch, C., Kang, S., Andersson, A., Chen, P., Zhang, Q., Cong, Z., Chen, B., Qin, D., and Gustafsson,
1086 Ö.: Sources of black carbon to the Himalayan–Tibetan Plateau glaciers, *Nature Communications*, 7,
1087 12574. <https://doi.org/10.1038/ncomms12574>, 2016a.



- 1088 Li, J. W., Han, Z. W., Wu, Y. F., Xiong, Z., Xia, X. G., Li, J., Liang, L., and Zhang, R. J.: Aerosol radiative effects
1089 and feedbacks on boundary layer meteorology and PM(2.5)chemical components during winter haze
1090 events over the Beijing-Tianjin-Hebei region, *ATMOSPHERIC CHEMISTRY AND PHYSICS*, 20, 8659-8690.
1091 <https://doi.org/10.5194/acp-20-8659-2020>, 2020.
- 1092 Li, Z., Lau, W. K. M., Ramanathan, V., Wu, G., Ding, Y., Manoj, M. G., Liu, J., Qian, Y., Li, J., Zhou, T., Fan,
1093 J., Rosenfeld, D., Ming, Y., Wang, Y., Huang, J., Wang, B., Xu, X., Lee, S. S., Cribb, M., Zhang, F., Yang, X.,
1094 Zhao, C., Takemura, T., Wang, K., Xia, X., Yin, Y., Zhang, H., Guo, J., Zhai, P. M., Sugimoto, N., Babu, S. S.,
1095 and Brasseur, G. P.: Aerosol and monsoon climate interactions over Asia, *Reviews of Geophysics*, 54,
1096 866-929. <https://doi.org/10.1002/2015RG000500>, 2016b.
- 1097 Liu, T., Gong, S., He, J., Yu, M., Wang, Q., Li, H., Liu, W., Zhang, J., Li, L., Wang, X., Li, S., Lu, Y., Du, H.,
1098 Wang, Y., Zhou, C., Liu, H., and Zhao, Q.: Attributions of meteorological and emission factors to the 2015
1099 winter severe haze pollution episodes in China's Jing-Jin-Ji area, *Atmos. Chem. Phys.*, 17, 2971-2980.
1100 <https://doi.org/10.5194/acp-17-2971-2017>, 2017.
- 1101 Liu, Y., Jia, R., Dai, T., Xie, Y., and Shi, G.: A review of aerosol optical properties and radiative effects,
1102 *Journal of Meteorological Research*, 28, 1003-1028. <https://doi.org/10.1007/s13351-014-4045-z>, 2014.
- 1103 Meehl, G. A.: Coupled Land-Ocean-Atmosphere Processes and South Asian Monsoon Variability, *Science*,
1104 266, 263-267. <https://doi.org/10.1126/science.266.5183.263>, 1994.
- 1105 Menon, S., Hansen, J., Nazarenko, L., and Luo, Y.: Climate Effects of Black Carbon Aerosols in China and
1106 India, *Science*, 297, 2250-2253. <https://doi.org/10.1126/science.1075159>, 2002.
- 1107 Morrison, H., Thompson, G., and Tatarskii, V.: Impact of Cloud Microphysics on the Development of
1108 Trailing Stratiform Precipitation in a Simulated Squall Line: Comparison of One- and Two-Moment
1109 Schemes, *Monthly Weather Review*, 137, 991-1007. <https://doi.org/10.1175/2008MWR2556.1>, 2009.
- 1110 O'Neill, N. T., Eck, T. F., Smirnov, A., Holben, B. N., and Thulasiraman, S.: Spectral discrimination of coarse
1111 and fine mode optical depth, *Journal of Geophysical Research: Atmospheres*, 108.
1112 <https://doi.org/10.1029/2002JD002975>, 2003.
- 1113 O'Neill, N. T., Pancrati, O., Baibakov, K., Eloranta, E., Batchelor, R. L., Freemantle, J., McArthur, L. J. B.,
1114 Strong, K., and Lindenmaier, R.: Occurrence of weak, sub-micron, tropospheric aerosol events at high
1115 Arctic latitudes, *Geophysical Research Letters*, 35. <https://doi.org/10.1029/2008GL033733>, 2008.
- 1116 Pokharel, M., Guang, J., Liu, B., Kang, S., Ma, Y., Holben, B., Xia, X. a., Xin, J., Ram, K., Rupakheti, D., Xin,
1117 W., Wu, G., Bhattarai, H., Zhao, C., and Cong, Z.: Aerosol Properties Over Tibetan Plateau From a Decade
1118 of AERONET Measurements: Baseline, Types, and Influencing Factors, *Journal of Geophysical Research:*
1119 *Atmospheres*, 124. <https://doi.org/10.1029/2019JD031293>, 2019.
- 1120 Qian, Y., Flanner, M. G., Leung, L. R., and Wang, W.: Sensitivity studies on the impacts of Tibetan Plateau
1121 snowpack pollution on the Asian hydrological cycle and monsoon climate, *Atmos. Chem. Phys.*, 11,
1122 1929-1948. <https://doi.org/10.5194/acp-11-1929-2011>, 2011.
- 1123 Qin, Y., and Xie, S. D.: Spatial and temporal variation of anthropogenic black carbon emissions in China
1124 for the period 1980–2009, *Atmos. Chem. Phys.*, 12, 4825-4841. [https://doi.org/10.5194/acp-12-4825-](https://doi.org/10.5194/acp-12-4825-2012)
1125 [2012](https://doi.org/10.5194/acp-12-4825-2012), 2012.
- 1126 Qiu, Y. L., Liao, H., Zhang, R. J., and Hu, J. L.: Simulated impacts of direct radiative effects of scattering
1127 and absorbing aerosols on surface layer aerosol concentrations in China during a heavily polluted event
1128 in February 2014, *JOURNAL OF GEOPHYSICAL RESEARCH-ATMOSPHERES*, 122, 5955-5975.
1129 <https://doi.org/10.1002/2016JD026309>, 2017.
- 1130 Rai, M., Kang, S., Yang, J., Chen, X., Hu, Y., and Rupakheti, D.: Tracing Atmospheric Anthropogenic Black
1131 Carbon and Its Potential Radiative Response Over Pan-Third Pole Region: A Synoptic-Scale Analysis Using



- 1132 WRF-Chem, *Journal of Geophysical Research: Atmospheres*, 127, e2021JD035772.
1133 <https://doi.org/10.1029/2021JD035772>, 2022.
- 1134 Ramanathan, V., Chung, C., Kim, D., Bettge, T., Buja, L., Kiehl, J. T., Washington, W. M., Fu, Q., Sikka, D.
1135 R., and Wild, M.: Atmospheric brown clouds: Impacts on South Asian climate and hydrological cycle,
1136 *Proceedings of the National Academy of Sciences of the United States of America*, 102, 5326.
1137 <https://doi.org/10.1073/pnas.0500656102>, 2005.
- 1138 Ramanathan, V., and Carmichael, G.: Global and regional climate changes due to black carbon, *Nature*
1139 *Geoscience*, 1, 221-227. <https://doi.org/10.1038/ngeo156>, 2008.
- 1140 Randles, C. A., da Silva, A. M., Buchard, V., Colarco, P. R., Darmenov, A., Govindaraju, R., Smirnov, A.,
1141 Holben, B., Ferrare, R., Hair, J., Shinozuka, Y., and Flynn, C. J.: The MERRA-2 Aerosol Reanalysis, 1980
1142 Onward. Part I: System Description and Data Assimilation Evaluation, *Journal of Climate*, 30, 6823-6850.
1143 <https://doi.org/10.1175/JCLI-D-16-0609.1>, 2017.
- 1144 Shi, Y., Bilal, M., Ho, H. C., and Omar, A.: Urbanization and regional air pollution across South Asian
1145 developing countries – A nationwide land use regression for ambient PM_{2.5} assessment in Pakistan,
1146 *Environmental Pollution*, 266, 115145. <https://doi.org/10.1016/j.envpol.2020.115145>, 2020.
- 1147 Skiles, S. M., Flanner, M., Cook, J. M., Dumont, M., and Painter, T. H.: Radiative forcing by light-absorbing
1148 particles in snow, *Nature Climate Change*, 8, 964-971. <https://doi.org/10.1038/s41558-018-0296-5>,
1149 2018.
- 1150 Smirnov, A., Holben, B. N., Slutsker, I., Giles, D. M., McClain, C. R., Eck, T. F., Sakerin, S. M., Macke, A.,
1151 Croot, P., Zibordi, G., Quinn, P. K., Sciare, J., Kinne, S., Harvey, M., Smyth, T. J., Piketh, S., Zielinski, T.,
1152 Proshutinsky, A., Goes, J. I., Nelson, N. B., Larouche, P., Radionov, V. F., Goloub, P., Krishna Moorthy, K.,
1153 Matarrese, R., Robertson, E. J., and Jourdin, F.: Maritime Aerosol Network as a component of Aerosol
1154 Robotic Network, *Journal of Geophysical Research: Atmospheres*, 114.
1155 <https://doi.org/10.1029/2008JD011257>, 2009.
- 1156 Srivastava, P., and Sharan, M.: An Analytical Formulation of the Monin–Obukhov Stability Parameter in
1157 the Atmospheric Surface Layer Under Unstable Conditions, *Boundary-Layer Meteorology*, 165, 371-384.
1158 <https://doi.org/10.1007/s10546-017-0273-y>, 2017.
- 1159 Sun, E., Xu, X., Che, H., Tang, Z., Gui, K., An, L., Lu, C., and Shi, G.: Variation in MERRA-2 aerosol optical
1160 depth and absorption aerosol optical depth over China from 1980 to 2017, *Journal of Atmospheric and*
1161 *Solar-Terrestrial Physics*, 186, 8-19. <https://doi.org/10.1016/j.jastp.2019.01.019>, 2019.
- 1162 Wang, P., Guo, H., Hu, J., Kota, S. H., Ying, Q., and Zhang, H.: Responses of PM_{2.5} and O₃ concentrations
1163 to changes of meteorology and emissions in China, *Science of The Total Environment*, 662, 297-306.
1164 <https://doi.org/10.1016/j.scitotenv.2019.01.227>, 2019.
- 1165 Wiedinmyer, C., Akagi, S. K., Yokelson, R. J., Emmons, L. K., Al-Saadi, J. A., Orlando, J. J., and Soja, A. J.:
1166 The Fire INventory from NCAR (FINN): a high resolution global model to estimate the emissions from
1167 open burning, *Geosci. Model Dev.*, 4, 625-641. <https://doi.org/10.5194/gmd-4-625-2011>, 2011.
- 1168 Wu, G., Liu, Y., Zhang, Q., Duan, A., Wang, T., Wan, R., Liu, X., Li, W., Wang, Z., and Liang, X.: The Influence
1169 of Mechanical and Thermal Forcing by the Tibetan Plateau on Asian Climate, *Journal of*
1170 *Hydrometeorology*, 8, 770-789. <https://doi.org/10.1175/JHM609.1>, 2007.
- 1171 Wu, J., Fu, C., Xu, Y., Tang, J. P., Wang, W., and Wang, Z.: Simulation of direct effects of black carbon
1172 aerosol on temperature and hydrological cycle in Asia by a Regional Climate Model, *Meteorology and*
1173 *Atmospheric Physics*, 100, 179-193. <https://doi.org/10.1007/s00703-008-0302-y>, 2008.
- 1174 Wu, J. R., Bei, N. F., Hu, B., Liu, S. X., Zhou, M., Wang, Q. Y., Li, X., Liu, L., Feng, T., Liu, Z. R., Wang, Y. C.,
1175 Cao, J. J., Tie, X. X., Wang, J., Molina, L. T., and Li, G. H.: Aerosol-radiation feedback deteriorates the



- 1176 wintertime haze in the North China Plain, *ATMOSPHERIC CHEMISTRY AND PHYSICS*, 19, 8703-8719.
1177 <https://doi.org/10.5194/acp-19-8703-2019>, 2019.
- 1178 Xu, B., Cao, J., Hansen, J., Yao, T., Joswia, D. R., Wang, N., Wu, G., Wang, M., Zhao, H., Yang, W., Liu, X.,
1179 and He, J.: Black soot and the survival of Tibetan glaciers, *Proceedings of the National Academy of*
1180 *Sciences*, 106, 22114. <https://doi.org/10.1073/pnas.0910444106>, 2009.
- 1181 Yanai, M., Li, C., and Song, Z.: Seasonal Heating of the Tibetan Plateau and Its Effects on the Evolution
1182 of the Asian Summer Monsoon, *Journal of the Meteorological Society of Japan. Ser. II*, 70, 319-351.
1183 https://doi.org/10.2151/jmsj1965.70.1B_319, 1992.
- 1184 Yang, J., Kang, S., Ji, Z., and Chen, D.: Modeling the origin of anthropogenic black carbon and its climatic
1185 effect over the Tibetan Plateau and surrounding regions, *Journal of Geophysical Research: Atmospheres*,
1186 123, 671-692. <https://doi.org/10.1002/2017JD027282>, 2018.
- 1187 Yao, T., Pu, J., Lu, A., Wang, Y., and Yu, W.: Recent Glacial Retreat and Its Impact on Hydrological
1188 Processes on the Tibetan Plateau, China, and Surrounding Regions, Arctic, Antarctic, and Alpine
1189 Research, 39, 642-650. [https://doi.org/10.1657/1523-0430\(07-510\)YAOI2.0.CO;2](https://doi.org/10.1657/1523-0430(07-510)YAOI2.0.CO;2), 2007.
- 1190 Yao, T., Bolch, T., Chen, D., Gao, J., Immerzeel, W., Piao, S., Su, F., Thompson, L., Wada, Y., Wang, L., Wang,
1191 T., Wu, G., Xu, B., Yang, W., Zhang, G., and Zhao, P.: The imbalance of the Asian water tower, *Nature*
1192 *Reviews Earth & Environment*. <https://doi.org/10.1038/s43017-022-00299-4>, 2022.
- 1193 You, Q., Min, J., and Kang, S.: Rapid warming in the Tibetan Plateau from observations and CMIP5
1194 models in recent decades, *International Journal of Climatology*, 36, 2660-2670.
1195 <https://doi.org/10.1002/joc.4520>, 2016.
- 1196 You, Q., Cai, Z., Pepin, N., Chen, D., Ahrens, B., Jiang, Z., Wu, F., Kang, S., Zhang, R., Wu, T., Wang, P., Li,
1197 M., Zuo, Z., Gao, Y., Zhai, P., and Zhang, Y.: Warming amplification over the Arctic Pole and Third Pole:
1198 Trends, mechanisms and consequences, *Earth-Science Reviews*, 217, 103625.
1199 <https://doi.org/10.1016/j.earscirev.2021.103625>, 2021.
- 1200 Zaveri, R. A., and Peters, L. K.: A new lumped structure photochemical mechanism for large-scale
1201 applications, *Journal of Geophysical Research: Atmospheres*, 104, 30387-30415.
1202 <https://doi.org/10.1029/1999JD900876>, 1999.
- 1203 Zaveri, R. A., Easter, R. C., Fast, J. D., and Peters, L. K.: Model for Simulating Aerosol Interactions and
1204 Chemistry (MOSAIC), *Journal of Geophysical Research Atmospheres*, 113, -. 2008.
- 1205 Zhang, M., Zhao, C., Cong, Z., Du, Q., Xu, M., Chen, Y., Chen, M., Li, R., Fu, Y., Zhong, L., Kang, S., Zhao,
1206 D., and Yang, Y.: Impact of topography on black carbon transport to the southern Tibetan Plateau during
1207 the pre-monsoon season and its climatic implication, *Atmos. Chem. Phys.*, 20, 5923-5943.
1208 <https://doi.org/10.5194/acp-20-5923-2020>, 2020.
- 1209 Zhang, X., Xu, X., Ding, Y., Liu, Y., Zhang, H., Wang, Y., and Zhong, J.: The impact of meteorological changes
1210 from 2013 to 2017 on PM2.5 mass reduction in key regions in China, *Science China Earth Sciences*, 62,
1211 1885-1902. <https://doi.org/10.1007/s11430-019-9343-3>, 2019.
- 1212 Zhang, X. Y., Zhong, J. T., Wang, J. Z., Wang, Y. Q., and Liu, Y. J.: The interdecadal worsening of weather
1213 conditions affecting aerosol pollution in the Beijing area in relation to climate warming, *ATMOSPHERIC*
1214 *CHEMISTRY AND PHYSICS*, 18, 5991-5999. <https://doi.org/10.5194/acp-18-5991-2018>, 2018.
- 1215 Zhang, Y., Gao, T., Kang, S., Shangguan, D., and Luo, X.: Albedo reduction as an important driver for
1216 glacier melting in Tibetan Plateau and its surrounding areas, *Earth-Science Reviews*, 220, 103735.
1217 <https://doi.org/10.1016/j.earscirev.2021.103735>, 2021.
- 1218 Zhao, B., Liou, K. N., Gu, Y., Li, Q. B., Jiang, J. H., Su, H., He, C. L., Tseng, H. L. R., Wang, S. X., Liu, R., Qi,
1219 L., Lee, W. L., and Hao, J. M.: Enhanced PM2.5 pollution in China due to aerosol-cloud interactions,



1220 SCIENTIFIC REPORTS, 7. <https://doi.org/10.1038/s41598-017-04096-8>, 2017.

1221 Zheng, B., Zhang, Q., Zhang, Y., He, K. B., Wang, K., Zheng, G. J., Duan, F. K., Ma, Y. L., and Kimoto, T.:

1222 Heterogeneous chemistry: a mechanism missing in current models to explain secondary inorganic

1223 aerosol formation during the January 2013 haze episode in North China. [https://doi.org/10.5194/acp-](https://doi.org/10.5194/acp-15-2031-2015)

1224 [15-2031-2015](https://doi.org/10.5194/acp-15-2031-2015), 2015.

1225 Zhong, J. T., Zhang, X. Y., Dong, Y. S., Wang, Y. Q., Liu, C., Wang, J. Z., Zhang, Y. M., and Che, H. C.: Feedback

1226 effects of boundary-layer meteorological factors on cumulative explosive growth of PM_{2.5} during winter

1227 heavy pollution episodes in Beijing from 2013 to 2016, ATMOSPHERIC CHEMISTRY AND PHYSICS, 18,

1228 247-258. <https://doi.org/10.5194/acp-18-247-2018>, 2018.

1229